UNIVERSITY OF BRISTOL

MASTERS PROJECT

High Pressure Microplasma in Diamond and Silicon Substrates

Author:
Alex Kershaw

Supervisor:
Paul May

A thesis submitted in fulfilment of the requirements
for the degree of Chemical Physics (MSci)

in the

CVD Diamond Group
School of Chemistry

April 2015

Running microplasma devices at higher gas pressures confers advantages in terms of increased electron densities and higher radiation output, making them more suitable for commercial applications. However, it has been difficult to manufacture microhollow cathode devices (MCHDs) for pressures higher than one atmosphere. These devices also have a shorter operating life, as high pressure operation induces sputtering and melting of the cathodes. This project examines the performance of diamond and silicon based devices with a range of geometries, operating under pressures of 0.1 to 9.5 bar.

A range of MCHDs were fabricated using electrically conductive, boron doped, p-type diamond, p-type or n-type silicon as the cathode. An intrinsic electrically insulating layer was grown on the cathode, to act as a dielectric layer. Glass was also investigated as an alternative to intrinsic diamond. A laser cut aperture, ranging from 100 - 300μm, was milled through the cathode and dielectric layers. Molybdenum was chosen as the anode material.

I-V curves were taken for all the devices operating in helium, under pressure ranges of 0.1-9.5 bar. The use of argon gas was also tested in the silicon based devices. The self-pulsing and normal modes were identified. Paschen curves were recorded for the MHCDs. The devices were found to follow Paschen's law, though at a higher V_b than the law would predict.

Capacitance measurements of a reference capacitor using a current chirp successfully showed the method was viable. The same method was used to measure the plasma sheath capacitance. This yielded a value of 120 nF, although the errors associated were too large for the value to be reliable. These were due to instability of the plasma during the 10 ms test period, plus oversimplification of the circuit model of the plasma.

Optical emission spectra were recorded. The gas temperature of the plasmas were between 400-600 K, similar to those reported elsewhere for low pressure operation. The gas temperature was found to rise slightly with plasma current.

Finally, a device with an array of two 100μm by 1000μm slits was fabricated. The I-V curves indicated that one slit would strike first at a lower voltage, impeding the second slit from striking, potentially due to slight differences in geometry between the two slits. Simultaneous plasma was difficult to achieve at frequencies below 1 kHz.

Contents

Chapter 1

Introduction

1.1 Plasma Overview

Plasma is the fourth state of matter (after solid, liquid and gas), which is characterised by the presence of free electrons, positive and negative ions, excited species and radicals, along with other neutral species such as atoms and molecules[1]. Although plasmas are made up from charged particles, they are described as quasineutral, as on average the net charge is neutral. Plasmas exist throughout the universe and are largely thought to be the most common state of matter[2]. There are many commonly observed examples of plasmas such as stars, lightning and the aurora borealis. Plasmas are generated by an input of energy, which can be from a variety of sources such as thermal, electric field or radiation to name a few[1]. If this energy is enough to dissociate electrons from the atoms, then a plasma can be formed. Due to the large number of charged species present in plasmas, the interactions are dominated by Coulomb interactions and exhibit several key electromagnetic behaviours such as Coulomb shielding[3]. Due to the presence of the free electrons and ions, plasmas are electrically conductive.

1.2 Discharge parameters

The plasma state requires different characterising parameters compared to the other three states of matter. The three fundamental parameters are particle density, species temperature and the steady state magnetic field[5]. As plasma is made up from charged particles the particle density of the different species is important. The temperature of the species is also a fundamental parameter where, T_e is the electron temperature and T_g is the gas temperature[4]. Although there are many other parameters, these can be derived from knowing these three fundamental parameters, such as debye length and plasma frequency. A variety of plasmas can been seen in 1.1.

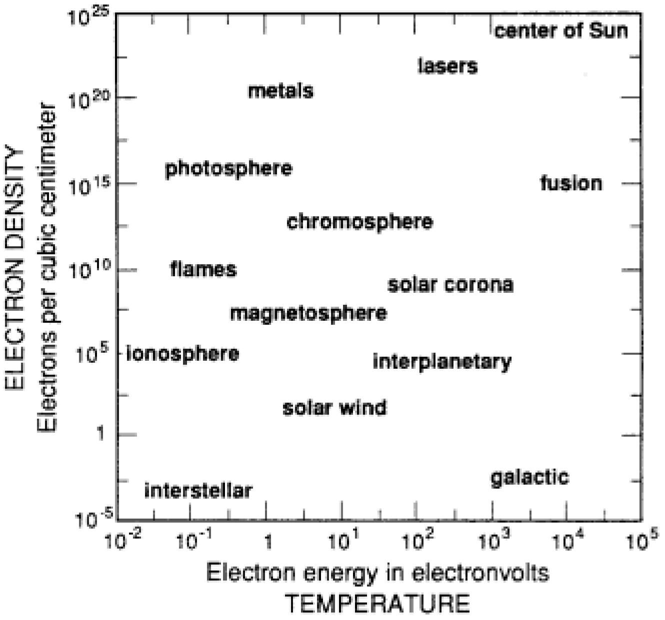

FIGURE 1.1: Plasma types as defined by the electron density and electron temperature[6]

1.2.1 Temperature of species

In non plasma conditions only the average temperature of all the species is considered. However as in plasmas some electrons are dissociated, they are able to travel with a different velocity to that of the ions and other heavier species. The electrons and ions behave differently in the electric and magnetic fields that are present in the plasma. Energy transfer between species with similar mass is efficient[7], causing the electrons will be in a thermal equilibrium, known as electron temperature, T_e. However as the ions and neutral species will have masses far greater than the electrons they may have a different temperature, known as gas temperature, T_g. This inefficient transfer of energy between the ions and electrons causes T_g to not be in equilibrium with T_e. The temperature is derived from the velocities of the particles, which have a Maxwellian distribution. For this assumption to be true the mean free path for the particle collisions must be much lower than the plasma container and the time between collisions must be much smaller than other time factors, such as heating rates[8]. Plasmas can be divided into two categories: thermal and non-thermal plasmas.

1.2.1.1 Thermal Plasma

Thermal plasmas can be generated by many different methods but at atmospheric pressure they are most commonly made by electrical arcs. One of the defining characteristics of thermal plasmas is that the electron energy distribution function is always assumed to be Maxwellian. As electron number density, n_e, is high and the electric field is weak, in thermal plasmas there is more transfer of energy between the larger species via elastic collisions. Thermal plasmas, because of this, are assumed to have T_g equal to T_e[9]. Thermal plasmas usually operate at much higher energies and gas temperatures than non-thermal plasmas and also generate more heat[1].

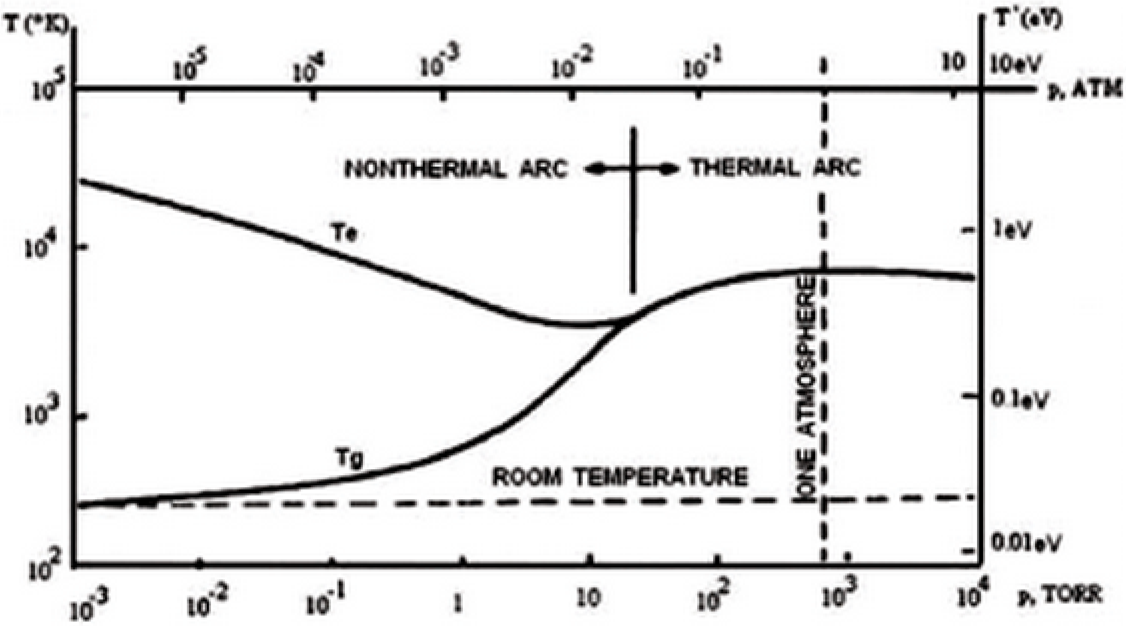

FIGURE 1.2: Electron and gas temperatures in an arc discharge plasma as a function of pressure[13].

1.2.1.2 Non Thermal Plasma

Non-thermal plasmas are usually driven electrically. The number of charged species is also often lower than in some thermal plasmas, such as arc discharges. This is because there is less energy available to promote the electron to a high enough energy level to become delocalised at a given temperature. The result of this is that the collisions between neutral and charged species play a larger part than in thermal plasmas. This combined with the preferential heating of the highly mobile electrons from the electric field result with $T_e \gg T_g$[4] as seen in figure 1.2. As the electrons receive preferential heating, the electron temperatures are high, around 104-105 K[1]. The high electron temperature allows reactions with high activation energies to occur which has significant impacts on industrial application such as ozone synthesis[10,11]. Another application of non-thermal plasmas in sensitive applications as a result of the relatively low gas temperature[1], such as in thin film photovoltaics using non-thermal plasmas to deposit silicon films[12].

1.2.2 Number density

The number density, n, of a plasma defines the charged particle density. The number density is given by,

$$n = n_e = n_i \tag{1.1}$$

where n_e is the density of free electrons and n_i is the density of ions. As the number of ions will be roughly the same as the number of ions it is only worth considering one of the densities. In a plasma n can be much lower than the neutral particle density. The relationship between the density of charged particles to neutral is given by the degree of ionisation , χ,

$$\chi = \frac{n_i}{n_n + n_i} \tag{1.2}$$

where n_n is the density of neutral particles[15]. The most frequently used number density expression for plasmas is the number of particles per Debye sphere, N_D, (a sphere with the radius of one Debye length, see section 1.2.3). N_D, is known as the plasma parameter.

1.2.3 Debye Shielding

Debye shielding is the short range shielding of the long ranged Coulomb interaction. While a plasma is quasineutral on the macroscopic scale, there can still be microscopic regions where significant charge densities can exist. The scale of these regions is given by the Debye length, λ_D. The electric potential can be calculated by assuming: the electron density, n_e, can be given by the Boltzmann distribution, which when solved using the Poisson equation gives,

$$\phi(r) = \frac{z \cdot e}{4\pi \cdot \epsilon_0} \cdot \frac{1}{r} \cdot exp\left(\frac{-r}{\lambda_D}\right) \tag{1.3}$$

where z is the charge on the particle and r is the distance away from the reference point[15]. In a non-thermal plasma, as $T_e \gg T_g$, the motion of the ions can be assumed to be static in comparison to that of the electrons. This gives the Debye length, from equation 1.3,

$$\lambda_D = \left(\frac{\epsilon_0 \cdot k_B \cdot T_e}{e^2 \cdot n_{e0}} \right)^{\frac{1}{2}} \tag{1.4}$$

which in laboratory plasmas typically have λ_D between 10μm - 200 μm[1]. The physical meaning of the Debye length has two forms. Firstly the Debye length is the distance at which the potential field falls to $\frac{1}{e}$ of its unshielded value. The second meaning is the distance at which a microscopic charge fluctuation is equal to the thermal energy[16].

1.3 Plasma Sheath

The electric field generated by the plasma, when confined in a vessel, has a significant role in the plasma physics. This effect occurs because of the plasma sheath, first noticed by Langmuir[18,19]. The electric field is strongest at the walls of the container due to the fast moving electrons. The electrons average velocity is much greater than the ions in the plasma, resulting in the electrons hitting the wall at a higher frequency than the ions do. Some of these electrons will be trapped in the wall creating a net negative region. This negative region has two effects on the charged particles in the remaining plasma. The other electrons will be repelled and the positively charged ions will be attracted, as shown in 1.3 . The positive region formed shields the quasineutral bulk plasma from negatively charged walls.

1.3.1 Sheath Thickness

The typical thickness of this wall is given by the electron Debye length[15]. Usually the debye length for the ions is much smaller than their mean free path, resulting in the sheath being near collision free[14]. However under equilibrium the sheath can only be maintained if the ions move with enough velocity at the sheath edge, known as the Bohm criterion[20,21]. The Bohm criterion requires that the ions are accelerated from the bulk to the sheath in a region known as the presheath[1]. If the presheath did not exist, the bulk plasma would only see a sheath edge and ions would not accelerate in the direction of the sheath.

The presheath thickness, L, where the scale of the presheath thickness $>>\lambda_D$, is usually determined by the ion mean free path or by the ionisation length. The presheath along with the plasma bulk are quasineutral while the sheath is not[22].

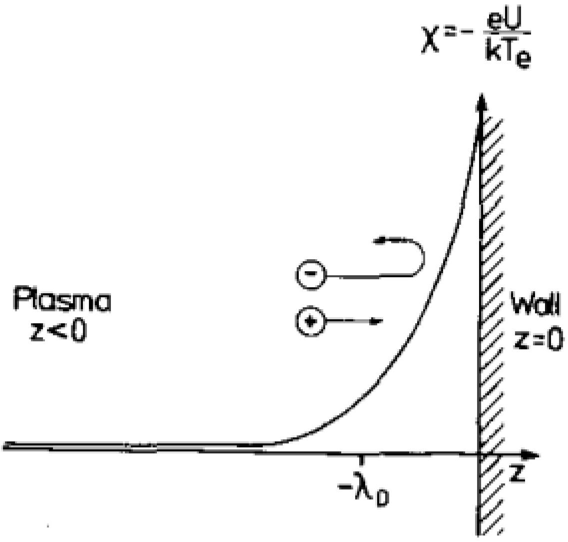

FIGURE 1.3: Potential of the plasma from plasma bulk to the wall, displaying the sheath. The attractions and repulsions of the electrons and ions are shown. Taken from Reimann[14].

1.3.2 Sheath Capacitance

As the plasma sheath is a region free from electrons, current will not readily flow through the sheath. The sheath therefore acts as a dielectric layer and will have a capacitance. The value of this capacitance relates to the overall thickness of the sheath[23].

1.4 Electric Plasma Discharges

The most common way to generate a plasma is by applying an electric field to breakdown a gas. Discharges are characterised by the behaviour of the electric field and are classified into three different types: DC, AC and pulsed discharges[30].

1.4.1 Townsend Mechanism

Townsend mechanism is a model describing the electric breakdown of a gas to form a plasma. When an electric field is applied across a gas, there is a build up of electrons at the cathode surface. Electrons are generated in the gas by energetic photons from an external source, such as cosmic radiation or from a radioactive source, causing a large electric field. The electrons built up at the cathode can leave the surface via field emission due to the large electric field present. These free electrons are then accelerated to the anode by the electric field between the electrodes. If the electric field is strong enough the electrons will be accelerated to a velocity where their kinetic energy is greater than the energy required to ionise another atom or molecule. If the high energy electron does collide and ionises a particle, two or more electrons will now be travelling towards the anode. This process forms an electron avalanche and is described by the first Townsend coefficient, α, where alpha is the gain per ionisation event. After this initial breakdown current can flow from the cathode to anode.

The second Townsend coefficient, β, originates from the positive ions in the electric field. After the electron has liberated a second electron a positive ion is left behind. The ion is accelerated in the opposite direction, towards the cathode. If the energy of the ion is large enough, when it collides with a neutral species, ionisation can occur. When a positive ion collides with the cathode surface, providing they have sufficient kinetic energy, secondary electrons can be produced. The production of secondary electrons at the cathode is described by the third Townsend coefficient, γ. The Townsend criterion for electric gas breakdown is given by equation 1.5,

$$\gamma[exp(\alpha \cdot d) - 1] = 1 \tag{1.5}$$

where d is the distance between electrodes[26]. In this equation β is ignored because of the low ionisation cross section compared to that of the electron-ion collision[32]. There is a minimum field strength required to accelerate the electrons and ions for the avalanche to occur, this potential is known as the breakdown voltage, V_b.

1.4.2 Paschen's Law

In 1889 Friedrich Paschen published a paper on the breakdown characteristics of plasmas created between parallel plates[27]. He empirically found that the breakdown voltage, V_B was varied with changes to both the distance between the plates, d, and the pressure of the gas, p. The relationship he discovered was,

$$V_b = \frac{B \cdot pd}{\ln{(pd)} + C} \tag{1.6}$$

where B and C are constants depending on the gas composition[28].

At $p{\cdot}d$ above the minimum V_B $p{\cdot}d$, there are more collisions between the electrons and the gas molecules across the gap due to the larger number of molecules between the electrodes. Although there are more collisions, the energy gained from each collision is less, requiring a higher voltage. At $p{\cdot}d$ below the $p{\cdot}d$ for the minimum V_B there may not be sufficient collisions to ionise enough gas molecules. The mean free path of the electrons for these low $p{\cdot}d$ values can come close to the distance between the electrodes. This results in the electrons not having enough collisions to form an avalanche even if the collisions are of a high energy[29].

1.4.3 DC Glow Discharges

Gas discharges at low pressures do not emit light at a constant intensity between the anode and cathode but instead give off characteristic regions of different light intensity. As seen in figure 1.4 there are several regions of interest along the tube. Next to the cathode is the cathode dark space or cathode sheath, where there is a strong electric field. The discharge is maintained in this region by the ions impacting on the cathode, producing secondary electron emission. This process creates a negative space charge. The region is dark as there is insufficient electron density to ionise the gas and start an electron avalance[30]. Next to the cathode dark space is the negative glow. This region is the brightest part of the plasma. After the electrons have been accelerated through the strong field present in the cathode dark space, they have a large amount of energy. These high energy electrons now have enough energy to ionise neutral species that they collide with increasing the number of charged particles. The overall region has a net negative charge but has the highest density of ions and electrons[31].

After the negative glow, the electron energy is much lower, as is the plasma density. This darker region is known as Faraday dark space[32]. The decrease in carriers is caused by a weak field between the presheath and the plasma bulk, causing the sheath to effectively expand across the whole width of the tube[33]. As the carrier densities are so low in Faraday dark space, the region is almost field free and therefore not many ionising event occur. Closer to the anode the field increases, again to the point where it is strong enough to accelerate electrons and ions to energies where ionisation can occur. This is known as the positive column, another bright region between the electrodes. In the positive column the rate of formation of ions and free electrons is higher than the rate of carrier losses to the walls. The positive column is usually the largest region and if the distance between the electrodes increases, the positive column is the only region to increase in size[34]. Finally, between the anode and the positive column exists a region where electrons are accelerated rapidly towards the anode and create the ions that enter the positive column creating photons[35].

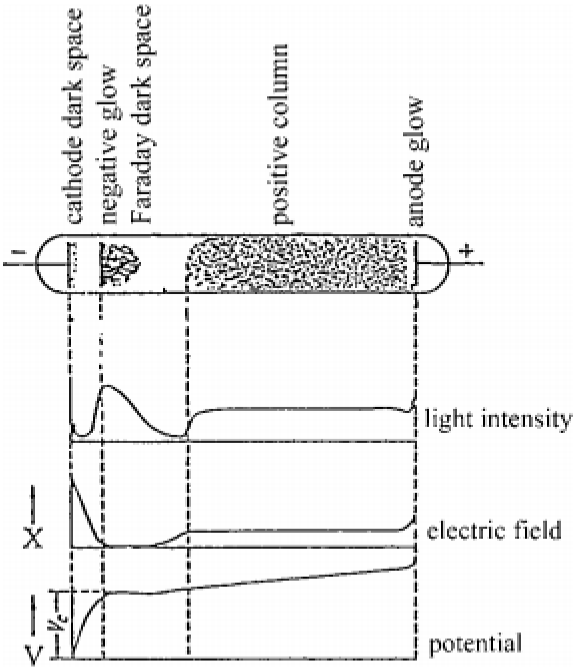

FIGURE 1.4: Glow discharge between two parallel plates with function of light intensity, electric field and potential, all as a function of distance. Taking from Francis[36].

1.4.4 Townsend and Glow Discharge

DC gas discharge plasmas are commonly described by their current-voltage characteristics. When the voltage between the anode and cathode reaches the breakdown voltage, a self sustaining discharge will be formed. If the current is not allowed to increase or the pressure is low enough such that no further avalanches can occur, the discharge is known as the dark or Townsend discharge, A-B in figure 1.5. The current densities of dark discharges are very low ($\leq 10^{-6}$ Acm^{-2})[1]. Few charge carriers are present as the electric field is too weak to generate a large carrier density. The contribution of the space charge, as a result of the low current density, to the field is often neglected as their impact is minimal[37]. The current contributions are almost entirely from the movement of background charges created from external events, such as cosmic rays. At A the current is saturated as all the background charges travel to the anode and cathode at the rate they are created, hence why an increase in voltage at A results in no increase in current. Little light is emitted during the Townsend discharge, hence the name dark discharge.

As the current is further increased, the plasma goes through a transition region which can be divided in two phases, the corona (between B and C) and the subnormal glow discharge between C and D. When the current is increased further, the normal glow discharge is formed. The discharge doesn't cover the whole cathode and an increase in current increases the area of the cathode covered by the discharge[15]. This is why the normal glow plateaus. If the discharge goes back to the Towsend mode, there is a hysteresis loop observed. With decreasing currents the plasma can sustain at lower currents than if the current was increased from the Townsend mode. If the current is increased further from the normal glow mode, then the whole cathode is covered and the discharge enters the abnormal glow mode. Increases in current, in the abnormal glow mode, result in an increase thickness of the cathode sheath[38].

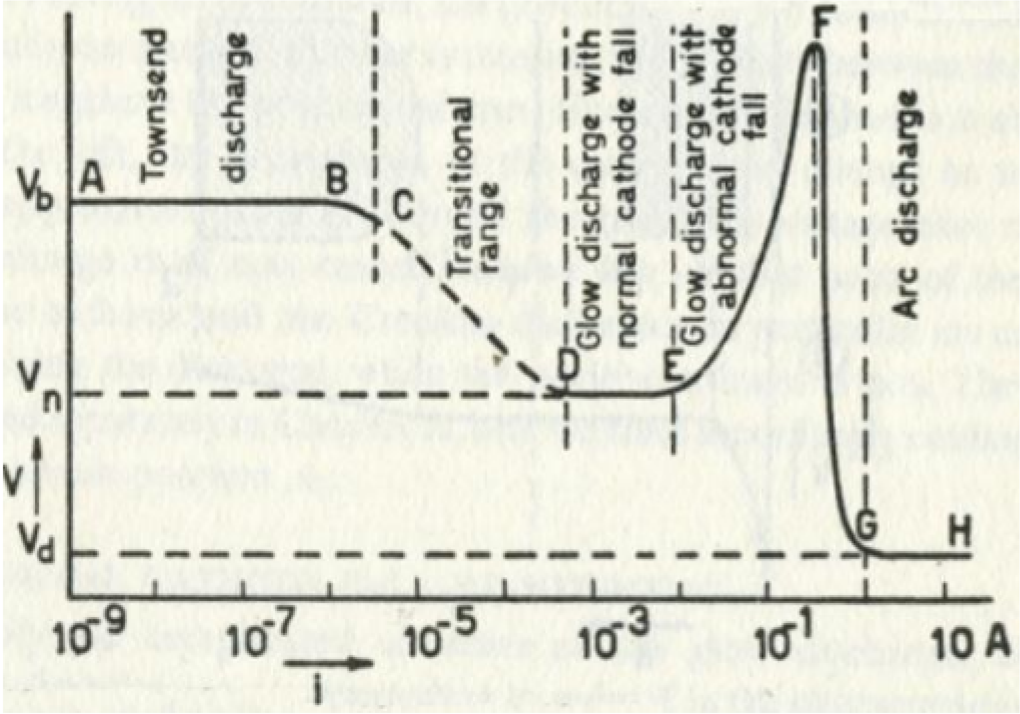

FIGURE 1.5: I-V curve of a gas discharge between two parallel plates, taken from Penning[39].

1.4.5 Arc Discharge

With increasing currents the ions collide with the cathode, providing more thermal energy to the electrode. If the current is high enough, the cathode will reach a temperature where there is enough thermal energy to excite electrons to the vacuum level, where they will be readily emitted. When the cathode undergoes thermionic emission, arc discharges begin to form[1]. Arc discharges operate at low voltages as can been seen at G in figure 1.5.

1.5 Microplasma

Microplasmas, or microcavity discharges, are defined as plasmas with a diameter of less than 1mm. Because of their small size, the pD scaling allows microplasmas to have more stability at much higher pressures than in larger discharges[40]. Despite the high pressures, microplasmas are still non-thermal plasmas[41]. A benefit of the high pressures is a high plasma density, even with low ionisation.

Microplasmas are often said to be collision dominated plasmas. The low ionisation degree means that the neutral species are much more abundant than the charged particles and as microplasmas operate at higher pressures, the rate of elastic collisions with neutral species is much higher than the inelastic charged particle collision rate[42].

1.5.1 Modified Paschen's Law

Paschen's law has been shown to only be valid for large values for electrode separation and low pressures. For extremely large or small values for $p{\cdot}d$ Paschen's law doesn't hold as true for microplasmas[43]. At atmospheric pressures, it was found that for $D < 10\mu$m V_B would deviate from Paschen's law and instead follow a modified Paschen's curve[44 45]. The modified Paschen's curve would continue to decrease linearly below the predicted V_B, as seen in figure 1.6.

At small $p{\cdot}d$ values it was found that electron field emission has a significant contribution and the plasma is no longer formed by the Townsend mechanism. Electron field emission is when electrons are emitted from a surface, usually in a vacuum, purely from the strength of the electric field, rather than from direct impacts supplying the energy. Kisliuk[47] found that, when $p{\cdot}d$ was below the Paschen curve minimum, at atmospheric pressures, ions that approached the cathode created a field strong enough for electron field emission to have a significant contribution to V_B. The rate of the electron field emission is independent of the rate of secondary electron emission, γ, meaning that any individual ion can contribute to either rate constant[48].

1.5.2 Device designs

Many different device designs exist to create microplasma devices, including dielectric barrier discharges, radiowave, microwave, microhollow cathode. The microhollow cathode design has several benefits, explained below, that make it well suited for high pressure operation. As the devices used in this report were a microhollow cathode design this section will focus on that type.

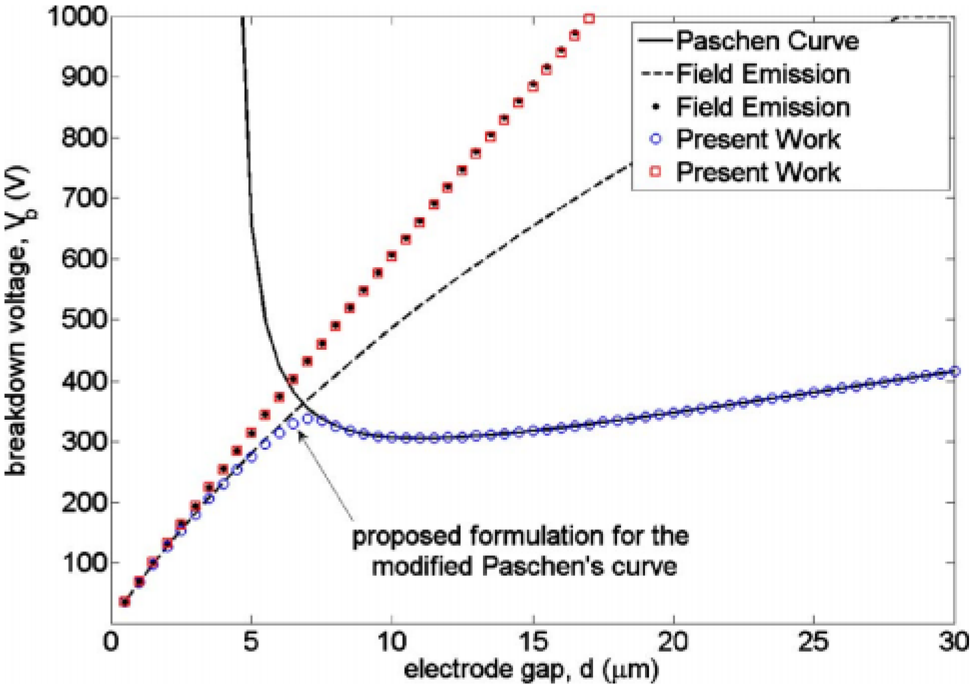

FIGURE 1.6: A modified Paschen curve for low electrode separation. Comparison is made with electron field emission[46].

1.5.2.1 Micro Hollow Cathode Device

The most common device design in literature is the microhollow cathode device, MHCD, first explored in the 1990s by Schoenbach et al.[49]. A hollow cathode device consists of a dielectric layer sandwiched between a conducting anode and cathode, with a hole through at least the cathode and dielectric layers. It has been well established that hollow cathodes can operate in a unique mode known as the hollow cathode mode[40].

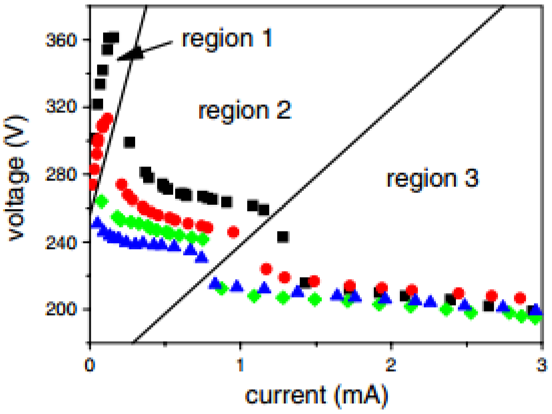

FIGURE 1.7: Three regimes of a MHCD shown on an I-V curve. At high pressures region one disappears[50].

There are three distinct regimes for MHCD, shown in figure 1.7. The first mode, existing at low currents, was once thought to be the predischarge mode but is now known to be the abnormal glow mode[51,56]. The abnormal glow mode is characterised by a large increase in voltage when the current is increased. The current can only increase with an increased rate of ionisation which requires a high sustaining voltage.

The second mode, the hollow cathode mode, is formed when the negative glow region is confined within the hollow cathode, occurring at low currents, but after the initial predischarge mode. As the current is increased past the abnormal mode, the electric field, which was once purely axial, now has a radial component. The electric field forms a potential trough in which electrons emitted from the cathode oscillate, where these electrons are known as pendulum electrons. The pendulum electrons were shown to exist by Helm in 1972[52]. The effective path length of these electrons is much larger, enabling more collisions within the same dimensions[53]. When the radial component forms, as the current is increased, there is a decrease in sustaining voltage of the plasma. When this negative differential resistance occurs on the V-I curve, the plasma is in the hollow cathode mode.

In the third mode, further increases in current result in the plasma expanding over the cathode surface outside the cavity. Further increases in current result in an increase in sustaining voltage and the plasma enters the abnormal glow mode, which has a positive I-V gradient[40].

MHCD's sustaining voltage not only scales with $p{\cdot}d$, as given in equation 1.6, but also scales with pD, where D is the diameter of the aperture in the cathode[54]. This scaling law is known as the White-Allis similarity law,

$$V_s = f(p \cdot D) \tag{1.7}$$

where V_s is the sustaining voltage and f is a loss factor[55]. This law suggests limits on the range of values (pD), for a plasma to operate in the hollow cathode mode, depending on gases used and device geometries, to around 1-10 Torr cm[40].

1.5.3 Electrode Materials

The material choice for the electrodes is critical for the successful operation of a microplasma device. The harsh environment around the plasma can sputter or react with the electrodes causing device failure.

1.5.3.1 Metals

Commonly used electrically conductive metals such a copper, silver and gold, as well as others have been used as the electrodes in devices. However, these metals have a relatively low melting point, so are only suitable for low pressure and low current(<1 mA) operation[57].

The most commonly used electrode material in literature is molybdenum. Due to the high thermal conductivity and one of the highest melting points of all elements[58], molybdenum is well suited as an electrode material. However molybdenum is still prone to sputtering when used in MHCDs[59].

1.5.3.2 Silicon

Silicon is a promising choice of electrode material for MHCDs. It has a very high melting point and a high resistance to sputtering[60]. It is also able to be produced on an industrial scale due to the large infrastructure available for the semiconductor industry. Whilst the silicon devices tested have run for tens of hours in literature, all the device have been limited to low pressure testing[61–63].

1.5.3.3 Diamond

Diamond has many appealing properties which make it viable for use for as the electrode material. Diamond has the highest melting point of all known materials[64]. It also has a large secondary electron emission efficiency[65]. These two features, along with many others properties such as being chemically inert, make it a suitable material for use in MHCDs. However literature contains few examples of the use of diamond for microdischarge devices. Chang et al.[66] found the use of diamond cathodes improved plasma illumination. The only diamond MHCD in literature was made by Mitea et al.[67]. They created two diamond devices. The first featured a p-type boron doped CVD diamond for the anode and cathode, plus an intrinsic diamond dielectric layer between them. The second featured metal electrodes either side of a diamond dielectric layer. At higher pressures or currents the discharges transitioned to an arc discharge causing the cathode to rapidly graphitise. However diamond as material showed potential for use in higher pressures, assuming the device design was changed.

1.5.4 Dielectric Materials

The dielectric layers in microplasma devices can also be made out of a wide range of materials. Materials such as ceramics have proven to be very effective for several reasons. First, they are able to cope with the high temperature requirements that atmospheric plasmas need. Ceramics are also commonly used in many modern electronic devices and there is a well established manufacturing infrastructure for integrating ceramics into devices[68] in high production volumes. Ceramics are also chemically inert, giving them good resistance to erosion from the chemically aggressive plasmas.

Many different types of ceramic have been used in literature. Mica is a common choice due to its low cost[49]. Multilayer devices created by von Allmen et al.[69] and Vojak et al.[70] used an electrical tape made primarily of alumina. This has the benefit of ease of manufacture but is only suitable for low temperature operation.

Other experiments have shown lower melting point materials such as plastics to be viable. One such example is PET[50].

1.5.5 Gases

Noble gases are virtually the only gases used in microplasma devices today. Noble gases are both very stable and chemically inert. They also form a plasma with a low gas temperature[41]. The ionisation energies of noble gases are very high and they form metastable species. Of the noble gases, helium is reported to form a stable plasma most easily, mostly due to its high thermal conductivity but also partly due to it having the highest ionisation energy at 24.59 eV[71].

Although the noble gases form a stable discharge most easily, other species have been used. One such example is supercritical CO_2[72].

1.5.6 Applications

There are several key benefits that microplasmas offer in comparison to ordinary plasmas:

- High electron density(up to $10^{15} cm^{-3}$)[40]
- Able to operate at atmospheric pressures and above
- The ability to manufacture low cost arrays

These properties show potential for microplasmas to be commercially viable in several different fields.

1.5.6.1 Destruction of VOCs

Certain environments, such as submarines and space stations, require processes to control the atmosphere composition. The removal of volatile organic compounds (VOCs) is important part of this control. Microplasmas have been successfully used to destroy up to 100% of certain molecules[73,74]. Another benefit microplasmas in this role is the high efficiency of the process, especially beneficial for use in the space industry.

1.5.6.2 UV Light sources

Plasma light sources are common throughout the world, usually as fluorescent tube light bulbs. However these conventional plasma light sources have several limitations; they usually contain mercury and they require fragile glass covers[75]. Microplasma light sources which emit UV light have been successfully manufactured[76,77]. These microplasma arrays were incased in a plastic casing which not only offer flexibility but they are also light weight. The lights covered areas up to 400 cm^2 and operate at pressures up to 700 Torr. With efficiencies of up to 30 lmW^{-1} these microplasma light sources are comparable to fluorescent tube lighting.

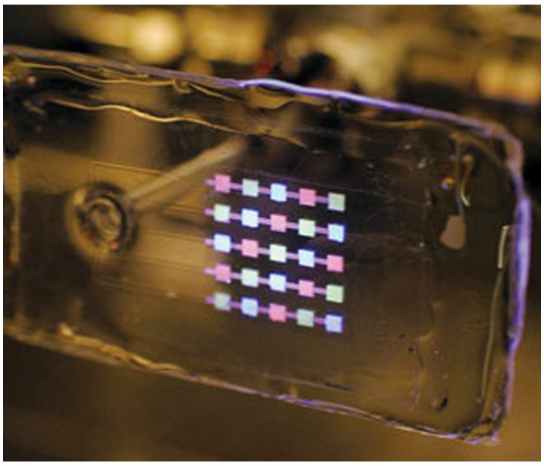

Figure 1.8: A flexible array of microplasmas emitting UV light excites a phosphor which emits visible light[75].

Chapter 2

Experimental

2.1 Sample Fabrication

The samples were fabricated individually for each microhollow cathode device.

Electrically conductive, boron doped, microcrystalline, p-type diamond was purchased from Element Six to make the diamond based cathodes. The diamond films were around 600μm thick, with an area of 10 mm x 10 mm.

For the silicon based cathodes, both n and p-type single crystal films with a similar thickness to the diamond films were used.

The anode was a molybdenum rod contained within the sample holder.

2.1.1 Diamond Growth

To create a dielectric layer on the cathode, the diamond samples were first washed in a solution of 3 M HCl and 4 M HNO_3 at 60°C for 30 minutes to remove any particles left on the surface from machining. The samples were then washed in acetone and seeded with microdiamond particles using a saline solution. The saline solution was made from poly(styrene sulfonate) (PSS), which contained a diamond suspension and poly(diallyldimethylammonium chloride) (PDDA) which is dispersed onto the sample before adding the PSS/diamond solution. The two polymers in the solution self-assemble resulting in the diamond nanoparticles sticking to the surface. They were then placed in a microwave CVD reactor, with up to four samples in at a time. The samples were positioned centrally below the plasma with the smooth side of the diamond samples facing upwards towards the plasma to ensure even and rapid growth. The flow rates for hydrogen and methane were 300 sccm(std. $cm^3\ min^{-1}$) and 8 sccm respectively. The flow rate of argon was found to have a negligible effect of the growth of the diamond films. The reactor was operated at a pressure of 100 Torr and the substrate temperature was kept to 1200 K. The growth rate of the intrinsic diamond was calculated to be 5 μm hour^{-1}. Samples were left to grow for a minimum of 10 hours, depending on the total required thickness of the dielectric layer. After being grown in the reactor, the samples were washed in the same acid solution for 30 minutes to remove any graphite remaining on the surface. To check the thickness of the dielectric layer was sufficient, an ohmmeter was used to measure the resistance of the sample to confirm the layer was insulating.

2.1.2 Sample Machining

The 10mm square samples were cut into four equal sized 5 x 5 mm samples using an Alpha series Nd-YAG micromachining laser (532 nm) manufactured by Oxford Lasers. The laser was used to cut at least a quarter of the way through the samples. The laser cut the smooth dielectric side of the samples at a rate of 5 mm s^{-1}, in the x-y plane, with a pulse distance of 10 μm. The laser was found cut at a rate of 2 μm s^{-1} in the z-direction. After laser cutting the samples were snapped along the laser cut grooves.

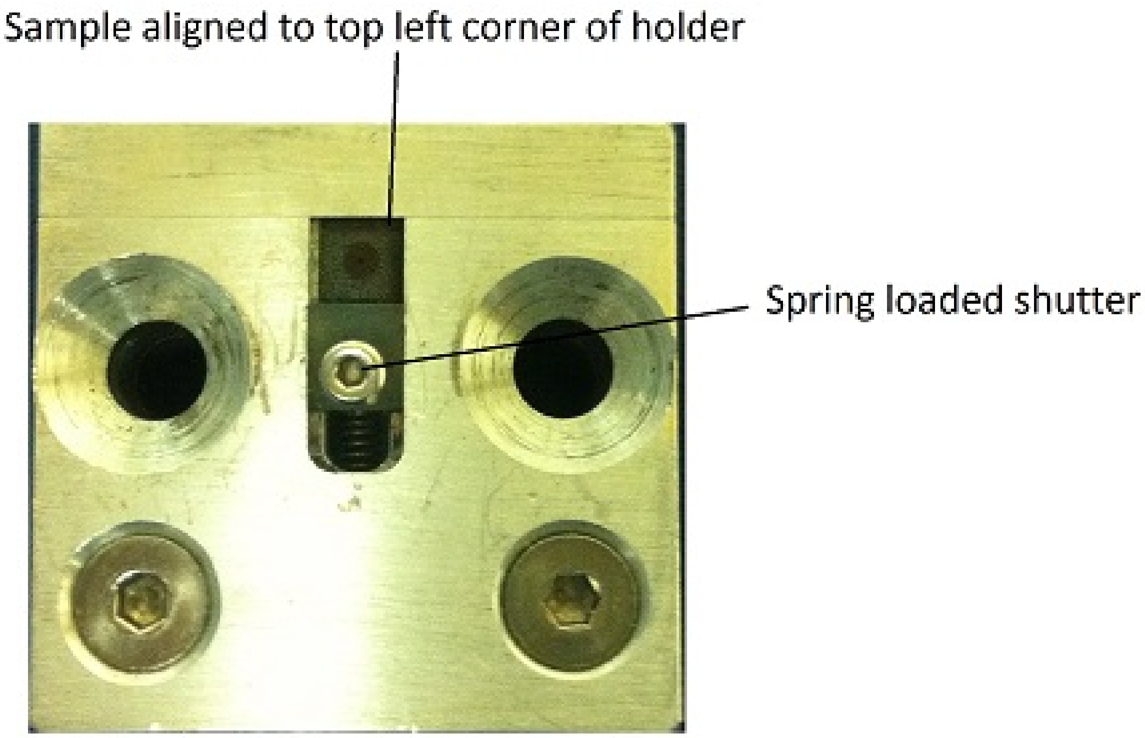

Figure 2.1: Sample holder used in the laser cutter to ensure holes aligned when milled from both sides.

To create a hollow cathode, an aperture was machined through the centre of the two layered diamond, the single silicon layered or the silicon-diamond cathodes. The laser cut the samples at a rate of 2mm s^{-1}, in the x-y plane, with a pulse distance of 10 μm initially through the smooth face. After cutting at least half way through the samples, they were rotated to have the rough side facing up. To make sure the holes were cut in the same position, the samples were placed in a sample holder which had a spring loaded shutter, as seen in figure 2.1. For small apertures, <150 μm, the laser would cut a cross like pattern on the underside of the sample. The double sided cutting was also done to achieve a uniform diameter throughout the samples as the laser tended to cut a smaller diameter hole through the lower side of the sample to that of the top. Diameters ranging from 50-300 μm were cut. After the milling the samples were examined under an optical microscope, up to 100x magnification, to examine the consistency of the holes cut. Finally the samples were washed in the boiling concentrated acid for one hour to remove any graphite formed from the laser cutting, then washed briefly in acetone before use.

For the silicon-glass samples, glass cover slips with thickness 130 μm were scored into 0.6 x 0.6 mm squares, then snapped along the scores. The glass was then glued to the silicon substrates, where the glue thickness was negligible. The silicon samples were only washed in acetone, as no graphite removal was required.

2.2 Sample Holder

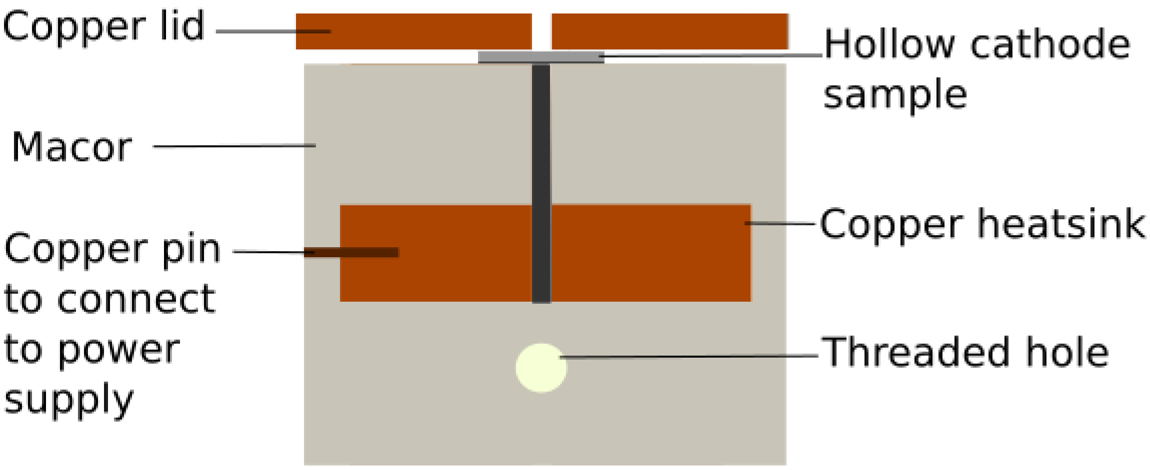

Figure 2.2: Schematic of the micro hollow cathode device sample holder.

The main sample holder, as seen in figure 2.2, was manufactured out of Macor, a ceramic which is easy to machine. The ceramic casing was also chosen as it is a good insulator for both heat and current. The Macor casing contained a copper heatsink, which was also used to supply current to the anode. The anode was made from molybdenum due to its high melting point, making it more resistant to sputtering than other accessible metals. The copper heatsink was connected to the power supply via a copper pin. To prevent arcing between the copper lid and the copper pin, the pin was surrounded in electrical tape and white tack. To provide current to the cathode, a copper lid with an aperture in the centre was place on top of the cathode. The samples were centred on the anode using a PTFE disk with a hole in the middle. This ensured the aperture in the cathode was centred over the anode.

2.3 High Pressure Chamber

All discharges were made in a stainless steel vessel, with a pressure tolerance of over 10bar. A quartz window on top of the steel chamber enabled vision of the discharges. Images of the vessel can be seen in figure 2.3. The removable Macor holder is held in place below the quartz window, centrally within the chamber.

After a sample was loaded, the chamber evacuated and the clamps attached, the chamber was purged with the required gas at least 3 times. The pressure gauge, made by Kobold (Man-SD3S), was accurate to ±1%. The chamber was connected to helium (up to 10 bar), Argon (up to 10 bar) and nitrogen(up to 1 bar). Most testing was done using helium as it was found to sputter the samples the least of all gases that were tested, for reasons discussed in section 1.5.5.

After extended use, the diamond samples were washed in concentrated HNO_3 at 100°C for one hour. This removed any graphite that was formed during operation.

2.4 Current-Voltage Testing

All testing on the microplasmas was done using a high voltage power supply made by Kepco (BOP1000M). The power supply was capable of operating in both current and voltage driven modes. The power supply was capable of producing voltages of ±1000 V and currents of ±40 mA. All testing was done under DC operation.

Connected to the power supply was a signal generator made by Stanford Research Systems (DS340). The signal generator could only produce triangular and saw tooth waves

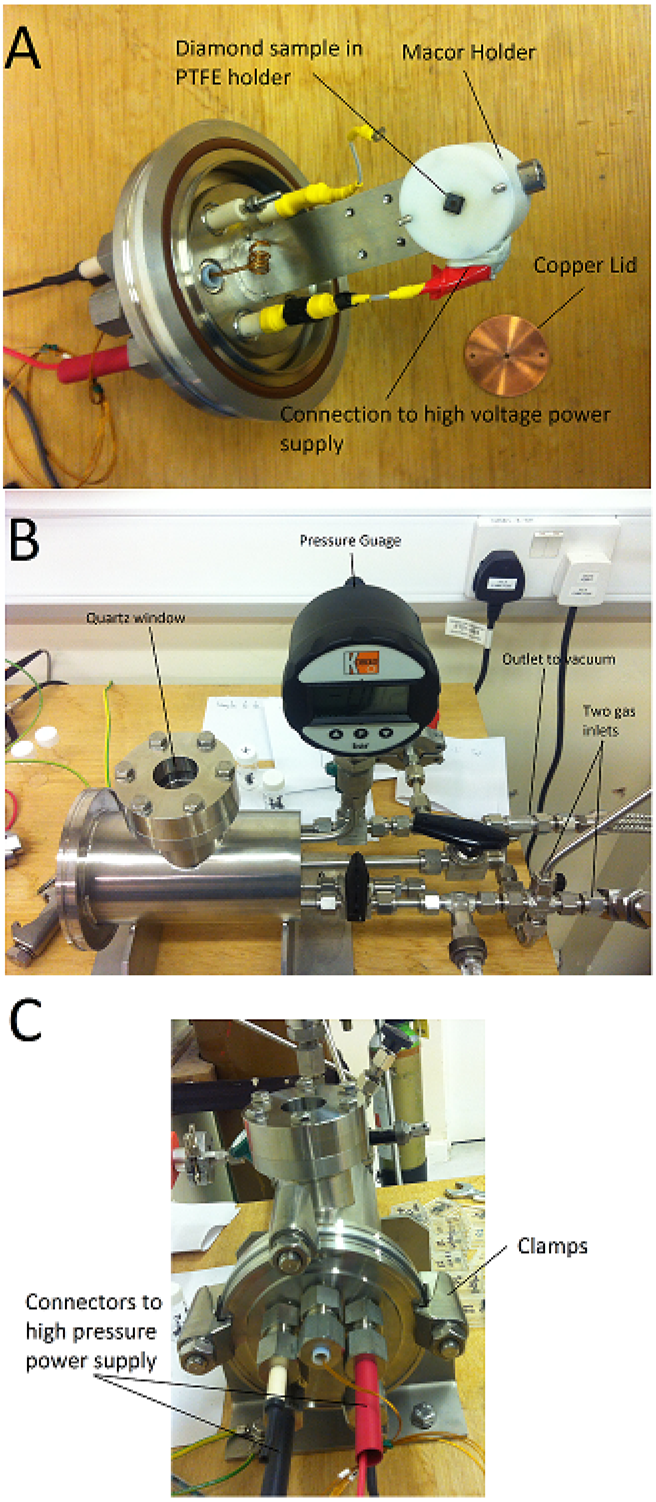

FIGURE 2.3: Image A is of a sample on the Macor holder. Image B is of the high pressure stainless steel chamber. Connections to the gas canisters are shown. Image C is the side view of the chamber. The wires connecting the MHCD to the high voltage power supply are shown

up to 1 kHz and sinusoidal waves up to 5 kHz, due to the limitations on the bandwidth of the power supply. The signal generator was also capable of sweeping across a predetermined range of frequencies at a defined rate.

2.4.1 Circuitry

The circuit of the experimental arrangement can be seen in figure 2.4, where the microplasma is modelled as a capacitor. Two probes, one high and one low voltage, were used to measure to current and voltage across the plasma. The voltage was given by the difference between the high voltage and low voltage probes. The current was calculated by dividing the low voltage probe reading by the 4.68 $k\Omega$ resistor, as given by Ohm's law. The resistor was added as a ballast resistor to increase the sensitivity in measuring small currents. The oscilloscope used was a LeCroy Waverunner 64Xi.

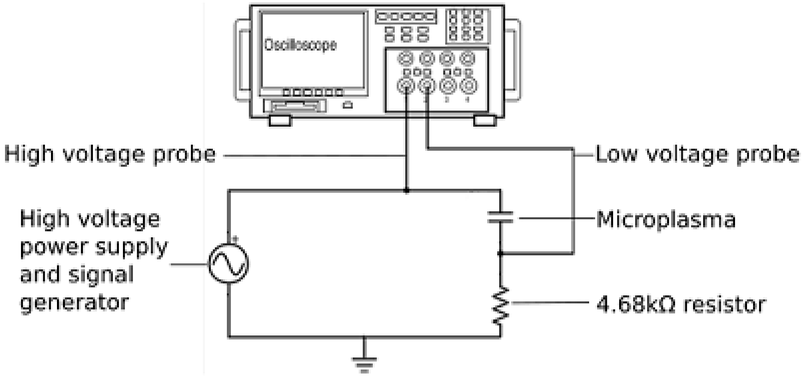

Figure 2.4: Circuit diagram of the MHCD arrangement.

2.4.2 I-V Curves

The I-V curves were recorded on the oscilloscope by plotting the current waveform against the voltage. The power supply was set to current driven mode and had a current range of 0-40 mA depending on the sample. For all I-V curves, a triangular waveform was used on the signal generator. The waveforms were averaged over 60 times to remove noise, except in certain cases where the averaging removed features, such as the double slit sample which will be discussed later. Each curve was saved with over 100,000 data points. Where applicable, the curves were smoothed using a Savitzky-Golay[78] filter with a decimation factor resulting in the number of data points being reduced to <30000 points.

2.4.3 Paschen Curves

To measure the breakdown voltages of the microplasmas, the power supply was set to voltage driven mode, with the current limits set to a maximum of 10 mA. The signal generator created a sawtooth waveform at 25 Hz with the breakdown voltage measured from a graph like the one seen in figure 2.5. Each breakdown voltage measurement was recorded >50 times and averaged to ensure more reliable data. The lowest pressure measurements were completed first, with the pressure increased via the gas inlet valve.

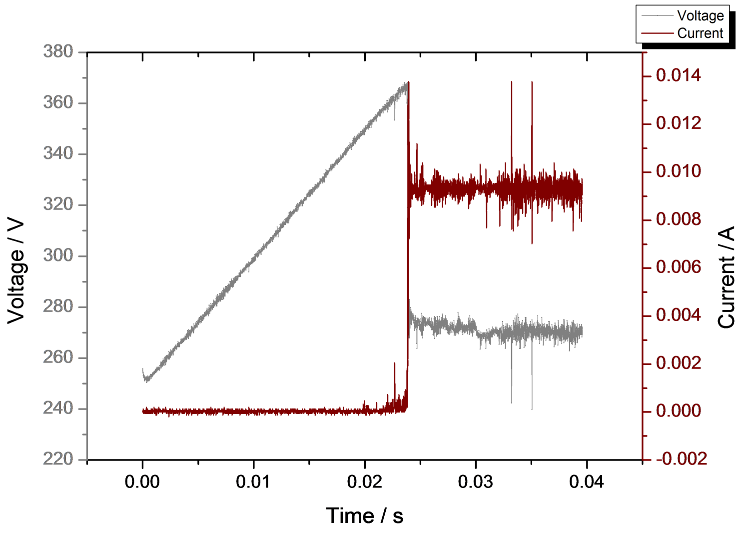

FIGURE 2.5: Current and voltage waveforms used to measure the breakdown voltage of a microplasma.

2.4.4 Capacitance Measurements

Measurements of the capacitance were first done using a 10 nF high voltage capacitor in parallel with a 12 $k\Omega$ resistor, as seen in figure 2.6. The power supply was set to current driven mode and the signal generator was set to create a chirp with a frequency rising from 50 Hz to 3 kHz. Each scan took 10 ms. The oscilloscope was set to AC coupling, as the amplitude of the waveforms was set to 0.15 mA, which was the smallest signal that the signal generator could produce. AC coupling was used as it allowed a large increase in resolution of the current and voltage waveforms saved.

To calculate the capacitance, the current and voltage waveforms were modelled. The current wave form was given by

$$I = a \cdot sin(\delta + 2\pi t(\alpha + \beta t)) \tag{2.1}$$

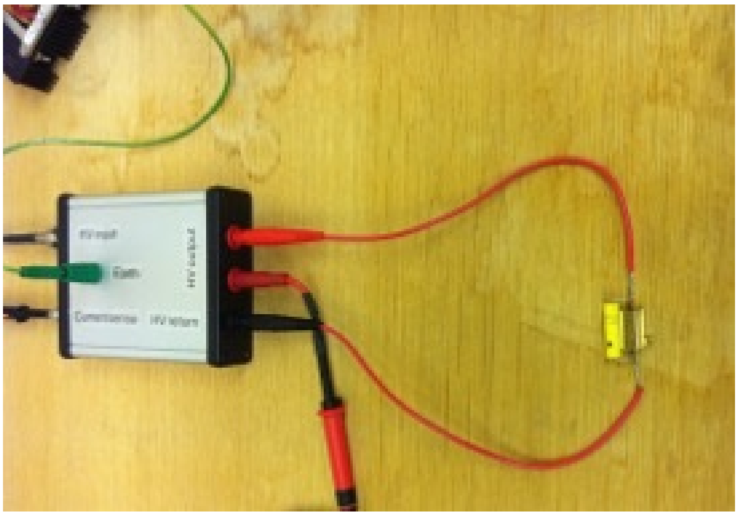

FIGURE 2.6: 10nF capacitor in parallel with a $12k\Omega$ resistor, used to calibrate capacitance measurements.

where a is the maximum current amplitude, δ is the phase difference between the current and voltage waveforms, α is the starting frequency of the chirp, β the final frequency with the time, t. The total impedance of a parallel circuit is the reciprocal of the components added and the reactance is given by,

$$X_c = \frac{1}{2\pi f C} \tag{2.2}$$

where f is the frequency and C is the capacitance. Current is related to voltage and impedance by an AC analogue of Ohm's law,

$$I = \frac{Z}{V} \tag{2.3}$$

When equations 2.1 and 2.2 are combined with equation 2.4

$$V = |V|e^{i(2\pi f t + \phi)} \tag{2.4}$$

this gives the voltage waveform to be,

$$\frac{V = ar(cos[2\pi t(\alpha + \beta t) + \delta] + 2\pi r C(\alpha + \beta t) sin[2\pi t(\alpha + \beta t) + \delta]}{1 + 4C^2 r^2 (\alpha + \beta t)^2} \tag{2.5}$$

Values for the capacitance and resistance were calculated using Wolfram Mathematica, where the constants were concurrently fitted for both the current and voltage waveforms.

For the capacitance measurements of the microplasmas, the oscilloscope was set to DC coupling to obtain an I-V curve. The current was then set to a value where the gradient of the I-V curve was flat to ensure no hysteresis effects were included, as discussed in section 1.4.4. After the current was set, the oscilloscope was set to AC coupling to record the chirp waveforms. To ensure there was no significant inductance in the cables, chirps were taken of a resistor which resulted in no measurable capacitance. All testing was done using helium gas at pressures between 3-5 bar.

2.5 Optical Spectroscopy

Optical emission spectroscopy was used to measure the gas temperature of the microplasmas. a Czerny-Turner spectrograph used was an EMCCD made by Andor Newton which had a focal length of 127 mm and a diffraction grating of 1800 mm^{-1}. A mercury pen lamp was used to calibrate the spectrometer, with the spectral lines used in figure 2.7. The chamber was purged 10 times before measurements were taken. Trace amounts of nitrogen were added to the chamber (<1%). Argon measurements were performed at a pressure of 0.5 bar and helium measurements at 1.5 bar. The exposure time was set to 2 seconds for each measurement.

Wavelength (nm)	Intensity
312.57	2800
313.17	2800
334.15	160
365.02	5300
365.48	970
366.3	650

FIGURE 2.7: Wavelengths of a mercury pen lamp used to calibrate the spectrometer. values taken from ref[79].

The spectra were taken between 366-392 nm. The spectra were simulated using the rotational, vibrational and electronic spectra fitting software PGOPHER[80], with bands taken from N_2, N_2^+ and CN. The three nitrogen bands were from its second positive system: $C^3\Pi_u$ (v=0) → $B^3\Pi_g$ (v=2),$C^3\Pi_u$ (v=1) → $B^3\Pi_g$ (v=3) and $C^3\Pi_u$ (v=3) → $B^3\Pi_g$ (v=4). The CN peaks were from its violet system: $B^2\Sigma^+$ (v=0) → $X^2\Sigma^+$ (v=0), $B^2\Sigma^+$ (v=1) → $X^2\Sigma^+$ (v=1), $B^2\Sigma^+$ (v=2) → $X^2\Sigma^+$ (v=2) and $B^2\Sigma^+$ (v=3) → $X^2\Sigma^+$ (v=3). The final peak was from the first negative system of N_2^+: $B^2\Sigma_u^+$ (v=0) → $X^2\Sigma_g^+$ (v=0). For the fitting, the concentration of each gas, each of the mentioned peaks and the rotational temperature were all varied for best fit. The gas temperature equal to the rotational temperature, assuming the helium or argon ions were in thermal equilibrium with the nitrogen molecules. A sample spectrum can be seen in figure

2.8. The measured spectrum can be seen on top, with simulations of the CN (blue), N_2^+(green) and N_2(black) below.

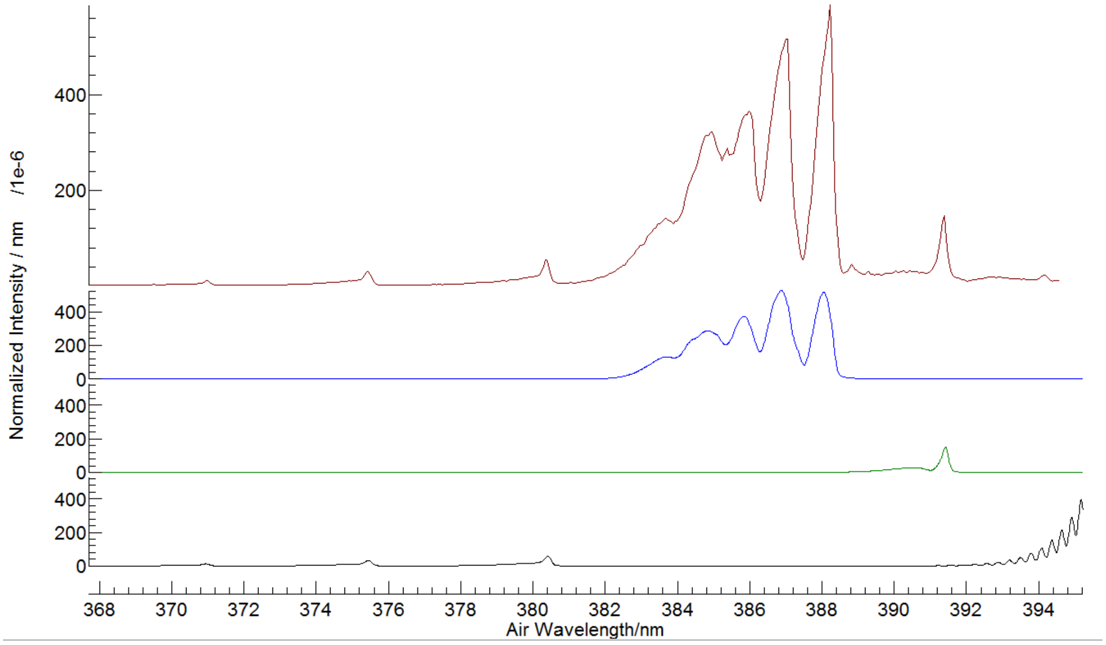

FIGURE 2.8: Optical spectrum of a helium plasma, used to measure gas temperature.

2.6 Imaging

Imaging of the samples was done using the Jeol JSM IT300 scanning electron microscope (SEM). The working distance was set to 50 mm. All samples and holders were washed in acetone before being placed in the SEM.

Chapter 3

Results and Discussion

3.1 Modes of Operation

All the MHCDs tested exhibited a similar I-V curve, independent of the aperture diameters used. An examples of these I-V curves can be seen in figure 3.1. Only two modes are shown in figure 3.1. The existance of the third mode, the abnormal glow mode, at higher pressures is questioned[51,56]. It does not appear to be present here, likely due to the plasma not fully covering the cathode at the pressures tested.

The self pulsing mode is visible between 0-1.2 mA in figure 3.1. The region, characterised by the negative differential resistance, shows the oscillation of the discharge current and voltage. The mode shown hear appears as a region of scatter points on the plot due to the time dependence of the mode. At low frequencies it was easy to see the confinement of the plasma within the aperture at low currents. At high currents, it was easy to observe the plasma spreading over the cathode surface, outside the hole.

For the setup used in figure 3.1, the normal glow discharge is shown at currents higher than 1.2 mA. A hysteresis loop was often observed within the normal glow mode. This hysteresis has been reported elsewhere and has been suggested to arise from the different rates of oscillations occurring after the self pulsing mode due to the expansion of the plasma[81–85].

3.2 Paschen Curves

Paschen curves for several 150 μm MHCDs are shown in figure 3.2. A model Paschen curve for helium gas is also plotted, with values taken from Burm[86]. Errors were calculated by using the standard deviation of the V_b measurements. As these were averaged

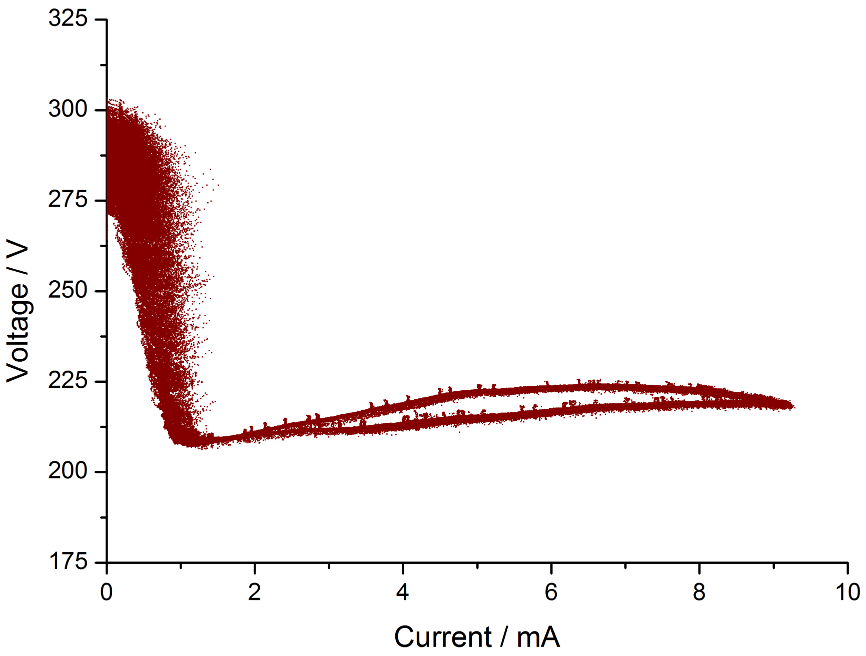

Figure 3.1: I-V curve of a 150 μm diamond based device operating at 1520 torr in helium. Two of the three modes are clearly visible, as is a hysteresis loop.

over more than 50 runs, this should be an accurate representation. The minimum pressures were limited by the plasma forming outside of the aperture and by limitations of the voltage output of the power supply. This is caused by the electrical connection to the anode being located in a direct path with the cathode. Even though the connections were thoroughly insulated with electrical tape and insulating putty, a plasma would often form outside the cavity. A new sample holder was designed but not fully manufactured, due to time constraints, that had the connections to the anode located on opposite sides of the device to the cathode connections. This design would prevent the plasma forming outside of the cavity and would allow lower $p{\cdot}d$ values to be explored.

The experimental curves are all at significantly higher breakdown voltages, with the breakdown minimum at a higher $p{\cdot}d$ than for the theoretical Paschen curves. There are several explanations for this. First, Paschen's law is defined for parallel plate discharge, not the MHCDs used here. As the plasma in MHCDs is located within the hollow cathode, not at the distance d, there would be an expected shift in the $p{\cdot}d$-axis. This shift for MHCDs is similar to the shift found by Sismanoglu and Amorima[87].

For $p{\cdot}d$ values below the minimum V_b, the MHCD has a much lower gradient than for the conventional parallel plate devices. This can be explained by the high ionisation efficiencies of MHCD designs due to the pendulum electrons. At low $p{\cdot}d$ values the

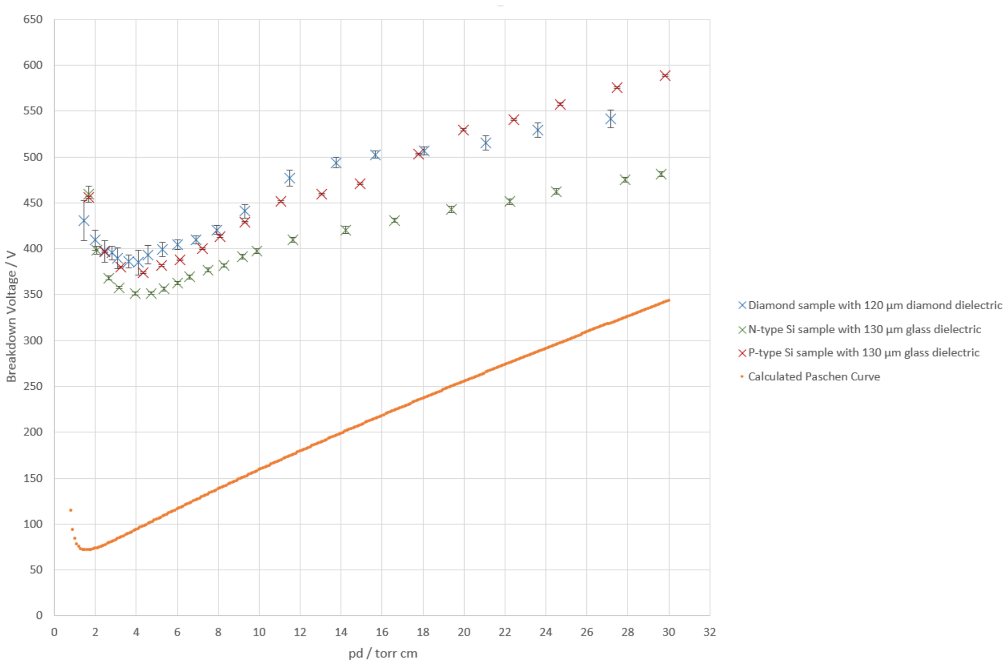

FIGURE 3.2: Paschen curves for three 150 μm devices made from diamond, N-type silicon and P-type silicon. The diamond device has a diamond dielectric layer whilst the two silicon devices have a glass dielectric layer. The simulated Paschen curve values are taken from Burm[86].

mean free path is long in comparison with d meaning higher voltages are needed to form the electron avalanches. As the pendulum electrons have a longer path length due to the hollow cathode, electron avalanches are easier to form at lower values for $p{\cdot}d$ than for the parallel plate discharge. Another factor contributing to the reduced gradient of V_b below the $p{\cdot}d$ minimum is the field emission effects as discussed in section 1.5.1, though these effects will be negligible due to the significantly larger value for d used here.

Interestingly, there was not a significant difference between the silicon and diamond samples. Due to diamond's high secondary electron emission efficiency, it was expected that plasmas would form with lower voltages. However the difference in V_b between the silicon and diamond samples was negligible.

3.3 Capacitance Measurements

Several methods were attempted for measuring the sheath capacitance, C, of the plasma in the sample devices. Each method was calibrated by measuring the capacitance of a known 10 nF capacitor in a parallel R-C circuit. One of the main difficulties was the small time period the plasma would be stable for.

3.3.1 Validation of Method

First the method of measuring the capacitance using a chirp needed to be validated by tests on a reference capacitor with a known value. A 10 nF high voltage capacitor was used, in parallel with a 12 $k\Omega$ resistor. This arrangement was chosen as it was thought to accurately mimic the circuitry of the microplasma[23]. The capacitor was first measured using the phase difference between the current and voltage waveforms, when the current input through the capacitor was a constant frequency wave form. It was measured at a value of 10 nF, to an accuracy of two significant figures.

After establishing the accuracy of the capacitor's quoted value, measurements were then attempted using a variable frequency current chirp. The simulation of the chirps can been seen in figure 3.3. The phase accuracy was very good, with less than 1% error. However the measured amplitude fit was slightly inaccurate. The current graph, at the top of figure 3.3, shows some of the source of this error. The signal generator was limited by the rate at which it could change frequencies, reducing the measured amplitude at higher frequencies. This results in values for C being 18.46 ± 0.72 nF, and gives a value for R of 12.5318 ± 0.000024 $k\Omega$. The quoted errors are much smaller than the actual deviation from the true values as this is not a random error but a systematic error stemming from the current supply. This systematic error is probably due to two factors. First, the current amplitude was assumed constant for all frequencies which has been found not to be the case. The second reason would be the distortion due to the rate at which the power supply could switch from high to low frequencies. However, these measurements were deemed accurate enough to attempt to obtain values for the microplasmas, as no literature values exist for microplasmas operating at these gas pressures.

3.3.2 Plasma Capacitance

Simulations of the chirp waveforms can be seen for both the current and voltage in figure 3.4. The value for C in this simulation was 120 ± 390 nF. It is clear from both the current and the voltage graphs that the simulation is not accurate. The phase of the current is consistently higher than the model predicts, which from equation 2.4 is vital for obtaining an accurate result for C. Another issue is the stability of the plasma over time period of the scan. At 5.5 ms in, as seen on the voltage graph, the plasma becomes unstable. However, due to limitations in the current waves created this time span could not be reduced.

Measuring the sheath capacitance via Langmuir probes, as commonly done in literature[88–92], would not be possible due to the size of the aperture. Also, interpretation of

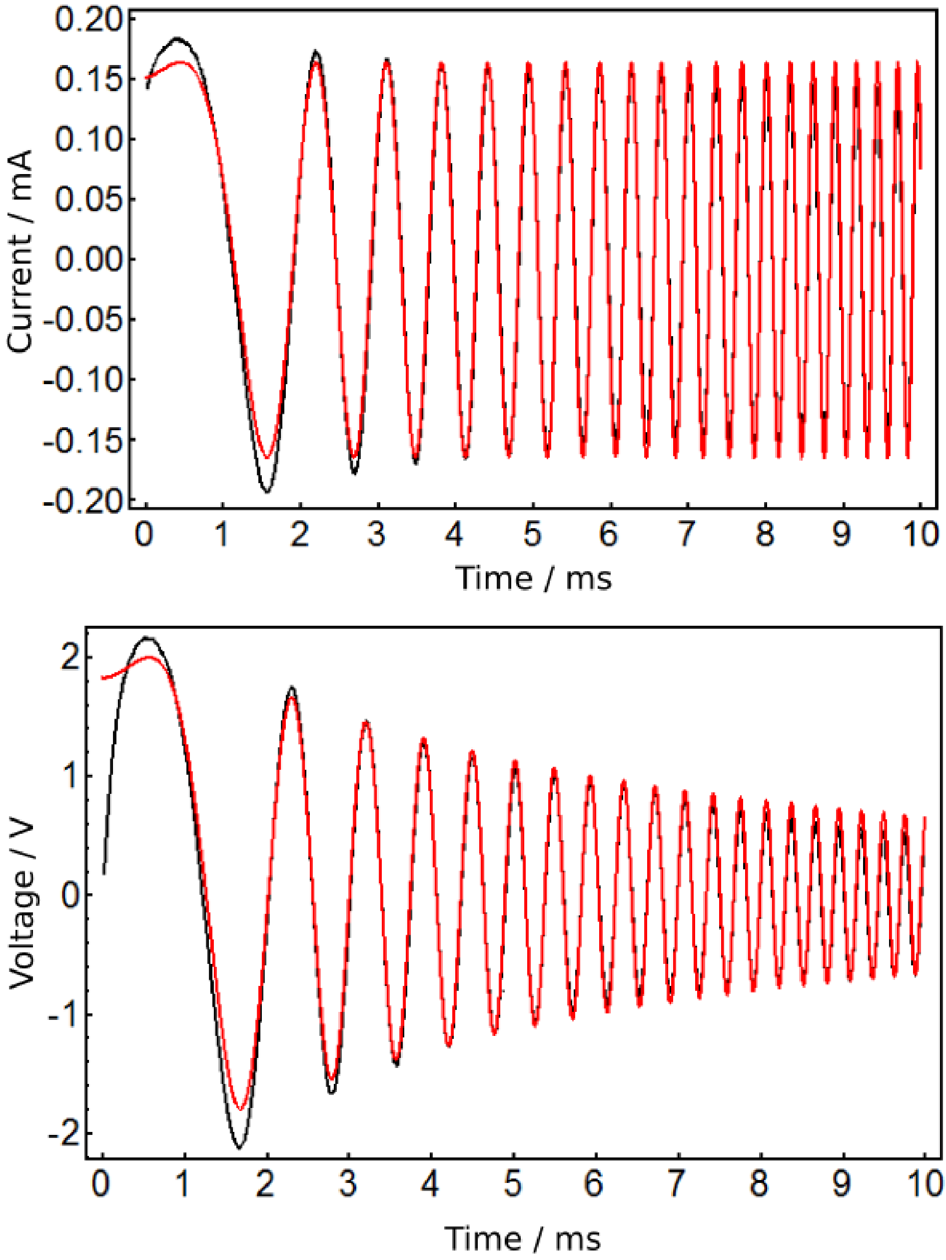

FIGURE 3.3: Simulations of the current and voltage chirps through a 10 nF capacitor in parallel with a 12 $k\Omega$ resistor, used to calibrate capacitance measurements. The red waveform is the simulation and the black waveform is the measured curve

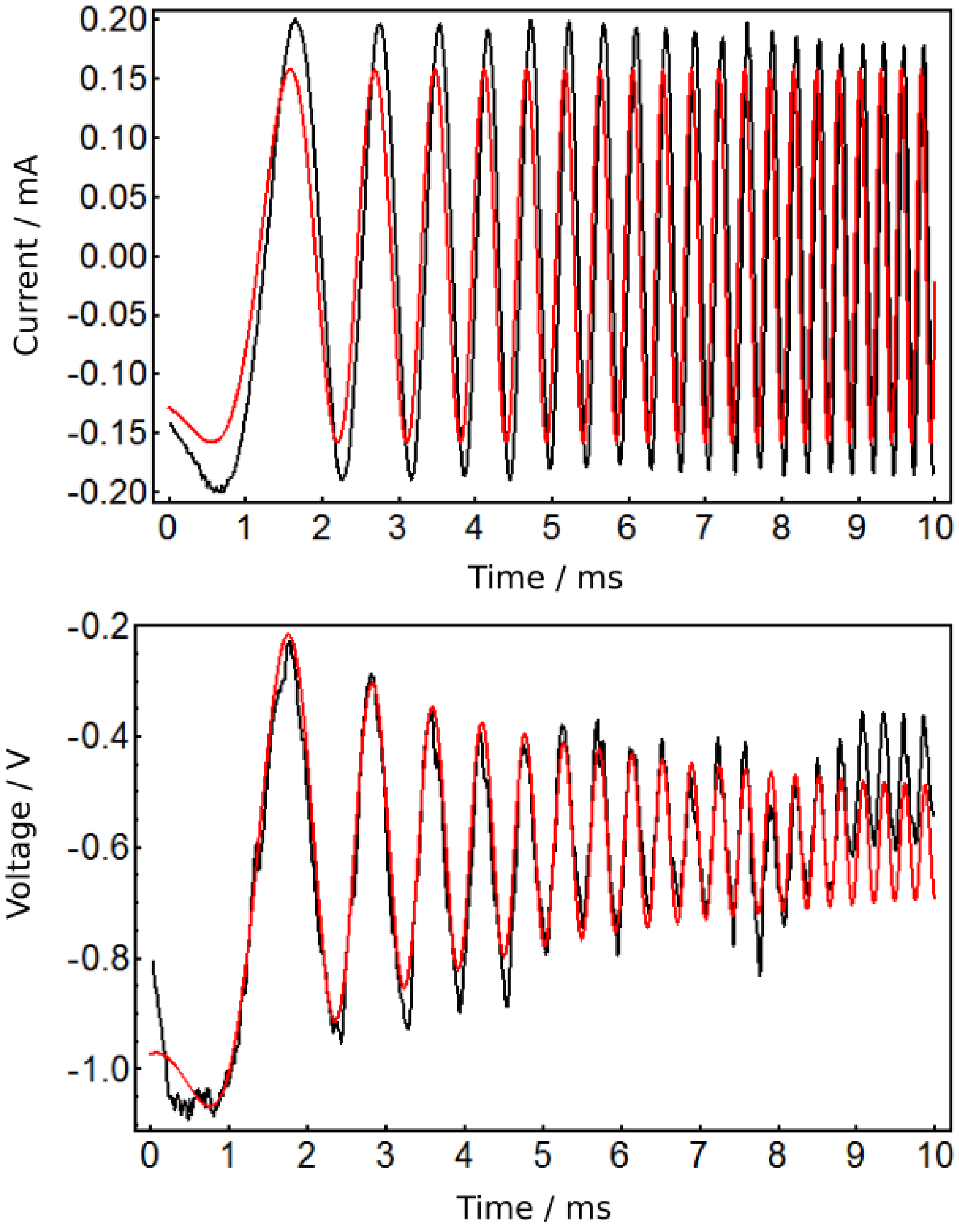

FIGURE 3.4: Simulations of the current and voltage chirps through a 150 μm microplasma in a diamond substrate, where the diamond dielectric layers average thickness was 120 μm. The gas used was helium at a pressure of 3.2 bar. The red waveform is the simulation and the black waveform is the measured curve

the results obtained by Langmuir probes in a non-thermal plasmas is complicated. An alternate method, viable in MHCDs, would be to measure the intensity of the ion optical emission spectra, as Lazzaroni et al. did[24,25]. Contrary to their report, at low pressures the plasma sheath was too small and as a result the sheath capacitance was too small to detect. For this reason the pressures used in this report were upwards of 2280 Torr in comparison to the maximum of 200 Torr employed by Lazzaroni et al.. Although Lazzaroni et al. used argon, a larger aperature and different electrode materials, the trend of decreasing sheath thickness with pressure would still be expected.

The error in C could be a result of oversimplifying the circuit model of the plasma sheath as a capacitor in parallel with a resistor. Instead, the circuit could be more like that assumed by Nation and Simpson[90], where there are multiple capacitors in both parallel and series, along with separate resistances for the plasma bulk and each sheath.

3.4 Array of Slits

For a large number of commercial applications, arrays are needed as they provide larger areas of microplasmas. However, when subjected to DC currents, both 3x3 and 2x2 arrays of 150 μm holes in diamond substrates would only have one aperture lighting up at a time. An array of two slits was fabricated, with dimensions of 1000x200 μm, as seen in figure 3.5. There was a slight misalignment of the laser when the samples were turned over, which resulted in the slits having slightly different geometries. The slits were operated in parallel without individual ballast resistors for each slit.

When tested, only one slit would light up at a time, consistent with the testing of the arrays of holes. The slits would tend to light up in a random sequence. At low pressures and high currents, the whole slit would be lit. However, with increasing pressures or decreasing currents, only a portion of the slit would be lit as the plasma retracted along the length of the slit. The plasma was much less stable at lower frequencies and the plasma would often re-strike until the frequency was at 1kHz or higher.

I-V curves of the array of slits can be seen in figure 3.6. The upper and lower curves represent the two slits. The slits operate at different voltages due to the slightly different geometries. After 1 mA, the devices enter the hollow cathode mode, as seen by the decreasing differential resistance. The I-V curve is similar to that of Wang and Ouyang[93], who used an alumina-mica-alumina sandwich design operated in argon at 20 Torr. Their I-V curve also had a constant negative differential resistance up to 8 Torr (the upper current limit of their experiment).

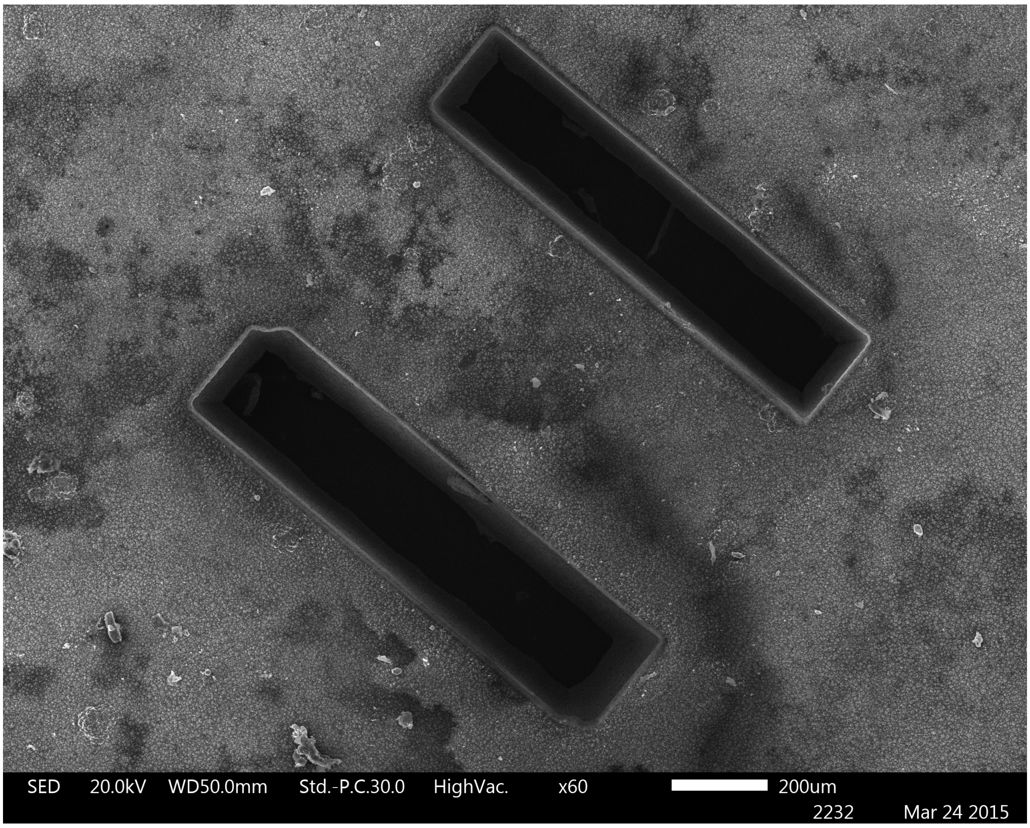

Figure 3.5: SEM image of a 2 slit array in a diamond substrate.

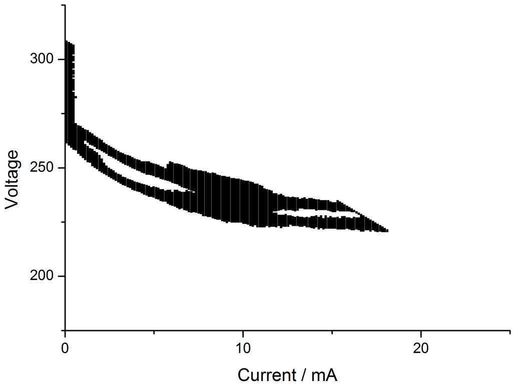

Figure 3.6: I-V curve of a 2 slit array in a diamond substrate. Measurements were taken at 760 Torr in helium at a frequency of 1 kHz.

3.5 Device damage

Understanding the mechanisms for the device failure is essential for using MHCDs in commercial applications. The failure mechanisms for both the diamond and the silicon devices were investigated. In both cases the dielectric material was left unharmed, whether it was made from glass or from intrinsic diamond, unlike the failure mechanisms found by Chen et al.[94]. In their experiments the dielectric layers laminated, preventing the cavities from striking. However, their failure testing was still to be completed.

3.5.1 Diamond Substrate

The diamond samples were able to survive over 10 hours of operation under moderate conditions (<5 bar of helium gas and <15 mA). After extended use, or if used under harsh conditions, the samples would begin to exhibit an Ohmic I-V characteristic, indicating a short circuit, as shown by the I-V curves. This ohmic behaviour was probably caused by the surface of the cathode turning to graphite when the plasma locally heated the diamond, converting it to its more thermodynamically favourable state[64]. This damage can be seen in figure 3.7. The samples were able to be reused after the graphite layer had formed if the samples were washed in heated, concentrated nitric acid for around 1 hour. The washed samples behaved in a similar fashion as before the graphitisation.

The shape of the aperture after use can be explained using the findings of Kushner[95]. In his modelling he found that the hottest electron temperatures, highest ion concentrations and the highest ionisation rates by secondary electrons were all focused on the cathode, immediately after the dielectric layer. This would cause the diamond to be sputtered most quickly adjacent to the dielectric layer, as found in all cases in figure 3.7. Interestingly, the rate of sputtering was found to increase with a thicker dielectric layer, although a larger range of dielectric layer thickness would need to be explored with more control on the operating conditions. This is probably caused by the increase in sustaining voltage required for samples with a thicker dielectric layer. This could result in increased rates of ionisation near cathode, increasing the impact rate at the diamond surface.

Device damage was not limited to the inside of the cathode aperture. The top surface of the samples also were affected by the plasma. There were two methods for this damage. When the plasma was operating in the normal glow mode, it would extend outside the cavity on to the top surface of the devices. This resulted in a sputtering of the surface as seen in figure 3.8. Another way in which the samples were damaged was via sputtering of the copper lid, shown in figure 3.9. When the plasma extended outside the cavity,

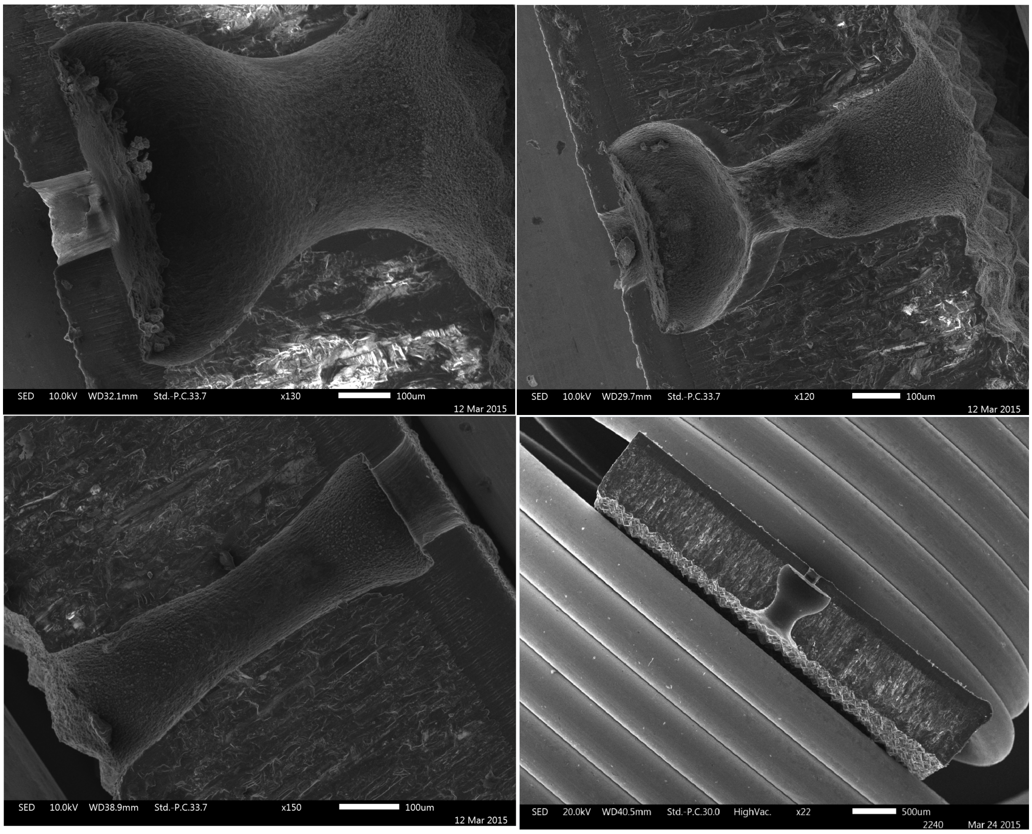

Figure 3.7: SEM image of the cross section of three different samples, together with an overview of the total cross section of a sample held in a spring. Top left: sample after over 10 hours of use, top right: sample with over 30 hours of use, bottom left: sample after around 2 hours of use. All samples were operated in helium gas with pressures up to 9.5 bar and currents up to 20 mA

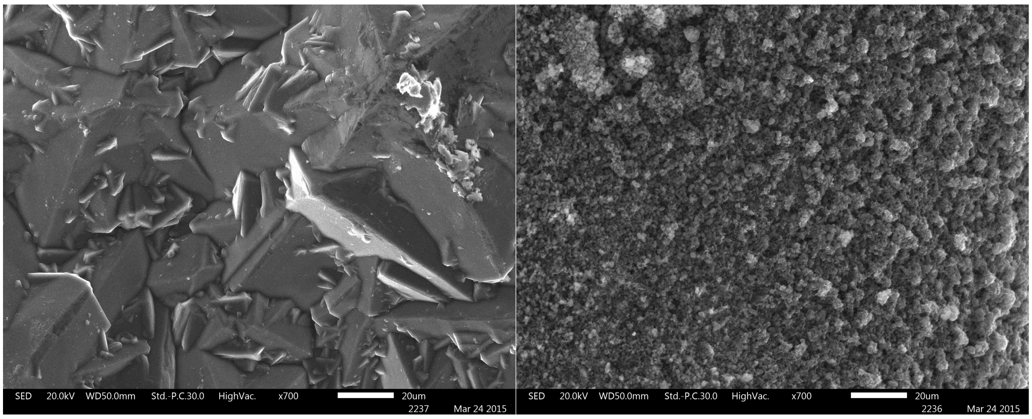

Figure 3.8: SEM image of the top surface of a diamond sample before(left) and after(right & below) over 10 hours of use in high pressure helium gas.

the plasma sputters the copper on to the surface of the samples. The light circular area in 3.9 is the region of sputter deposited copper.

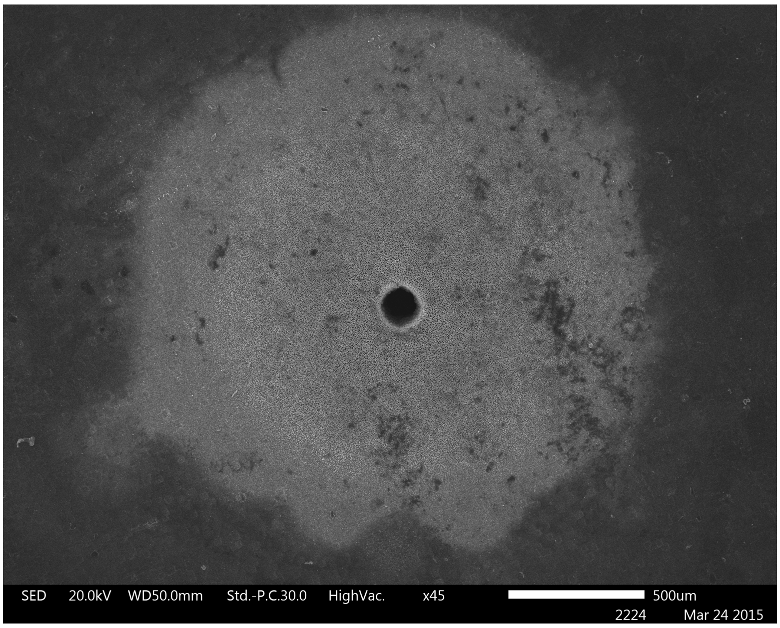

FIGURE 3.9: SEM image of the top surface sample showing the copper sputtering.

Continued use of the diamond samples, even in harsh conditions, could be viable if the anode also had an aperture. This would allow gas flow through the device, via thermal convection, preventing large build ups of graphite at the base of the device. This would also inhibit graphite from settling on the walls of the diamond, preventing the short circuit from occurring.

3.5.2 Silicon Substrate

The failure mechanism of the silicon devices is very different to the mechanism for diamond. As silicon has a much lower thermal conductivity than that of diamond, the single crystal devices locally melt. When the silicon solidifies again it reforms as polycrystalline silicon. As seen in figure 3.10 this melting and solidifying process is not the only process occurring. Felix et al.[96] also reported this porous texture on silicon devices that were used in a helium atmosphere, though at much lower pressures. Two mechanisms have been shown to exist for the destruction of the silicon surface, blistering due to helium implantation[97] and silicon ejection. In the devices examined here, the most prevalent mode is the silicon ejection. As the pressures used here were high, the silicon ejected at a relatively fast rate to that found by Felix et al.. This meant that the surface blistering, if present at all, would be destroyed by the silicon ejecting from the surface. The porous structure likely occurs when the silicon is locally melted due a current spike, based off the findings of Felix et al.. This hot melted silicon is then ejected from the surface, leaving behind a hollow cavity.

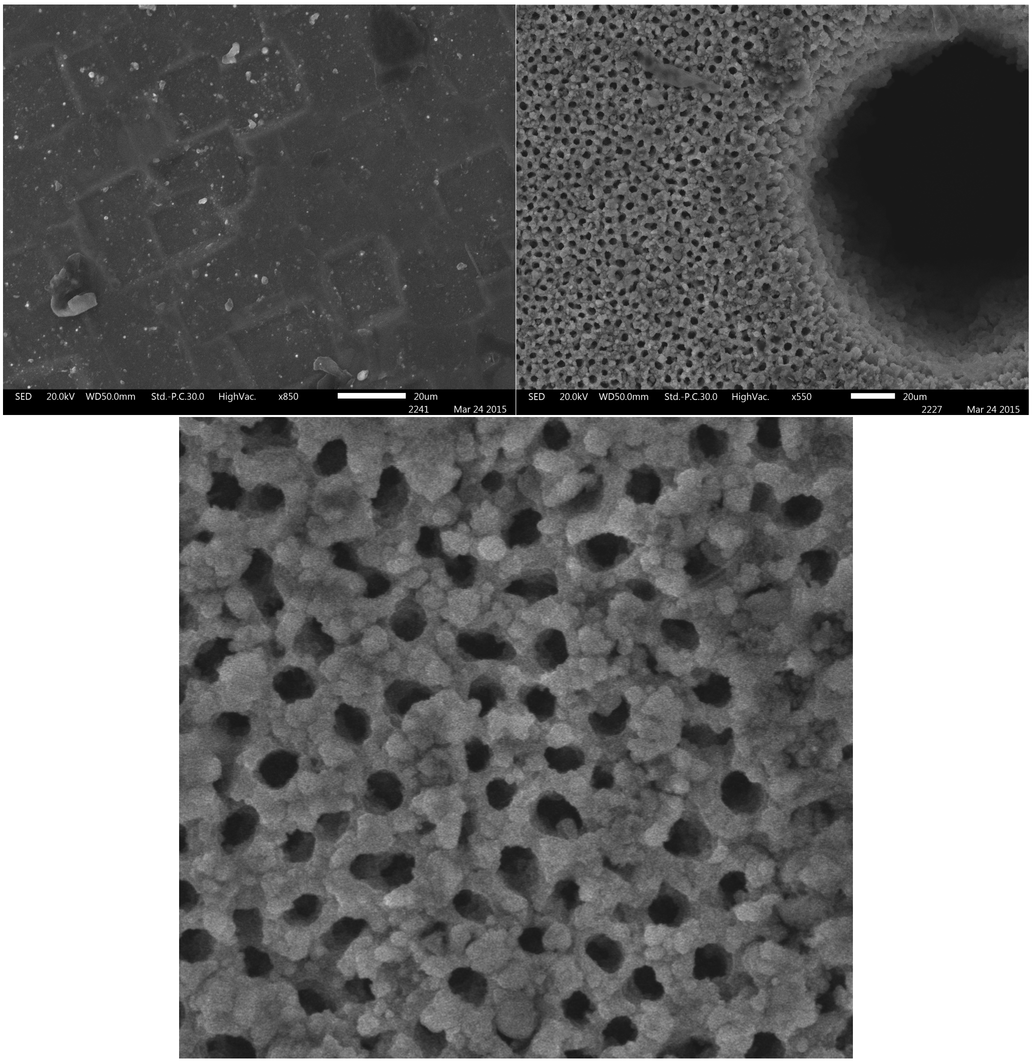

Figure 3.10: SEM image of the top surface of a silicon sample before(left) and after(right & below) several hours of use in high pressure helium gas. Ejection of the silicon due to the helium is clear on the right and lower images. The lower image is taken from the right image with an increased magnification.

Unlike the relatively efficient conversion of diamond to graphite, the silicon etched at a much slower rate, as seen in figure 3.11. After around 10 hours of use, with currents up to 40 mA and pressures up to 9.5 bar, the cylindrical aperture has hardly increased in diameter from its original size.

Rather than becoming ohmic, like the diamond samples, the silicon devices would start to require an increase in voltage to breakdown. The devices would also increasingly re-strike during operation. This is probably because the previously conducting doped single crystal layer has melted, causing the dopant atoms to accumulate. Once the dopant atoms are no longer dispersed throughout the sample, the silicon no longer is

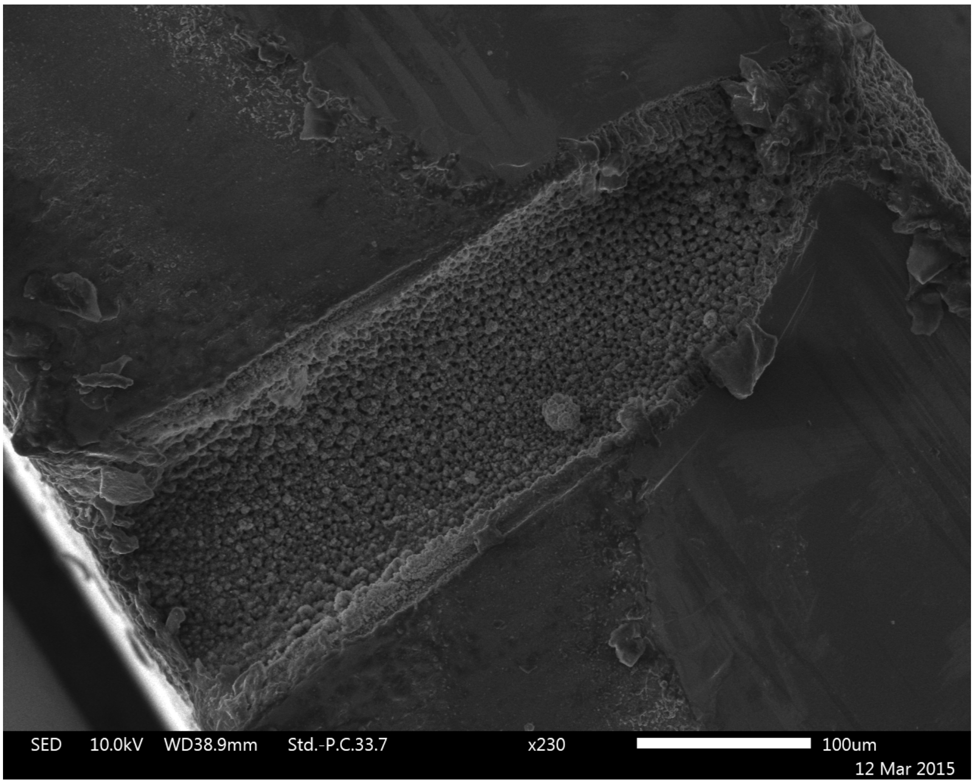

FIGURE 3.11: Cross section view of a 150 μm silicon device with the glass dielectric layer, that was on the top right of the image, removed. Note that the sample was milled by around 100 μm and then snapped. This sample did not cleave perpendicular to the face of the sample so the aperture appears to narrow.

electrically conductive as will act as a dielectric layer where the hollow cathode previously was. To refresh the samples, it may be possible to etch the polycrystalline layer using a substance known to etch silicon such as SF_6[96].

3.6 Gas Temperature

Measuring the gas temperature by using optical spectroscopy to calculate the rotational temperature, T_r, of nitrogen as a trace gas has been reported before[98,99]. T_r can be assumed to be in equilibrium with T_g, assuming the rotational states have a Boltzmann distribution[102], which were found to have a Boltzmann distribution in our experiments. In our measurements, N_2^+, N_2 and CN all gave similar temperatures when simulated individually, showing they are in partial thermodynamic equilibrium. This equilibrium only applies at the region measured and not throughout the whole plasma. This is contrary to the findings of Kurunczi et al.[99], who found the significant difference in T_r between N_2^+ and N_2. The assumption that T_g is in fact equal to T_r appears valid, given that the nitrogen is in partial thermodynamic equilibrium with the other gases and that the lifetime of the excited species is long enough, in comparison with the collision frequency, to form a Boltzmann distribution.

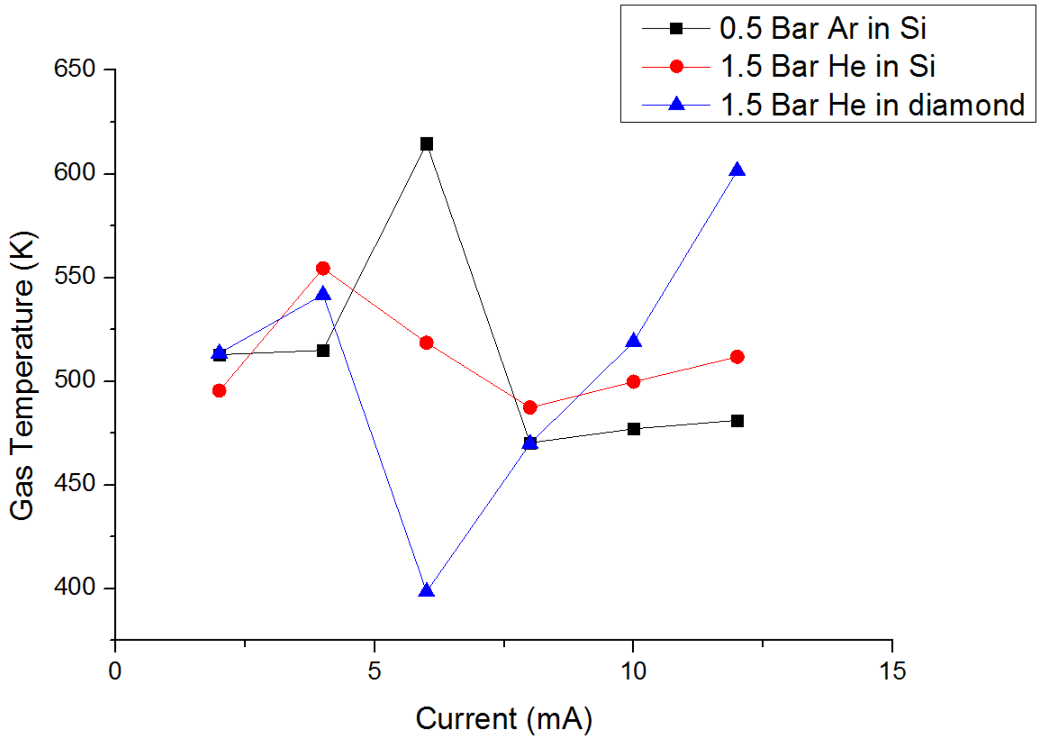

FIGURE 3.12: Comparison of the gas temperature in a plasma as the current is varied. Plots for both argon and helium in diamond and silicon substrates are shown.

Results of the effect of current on T_g can be seen in figure 3.12. It was expected that T_g would increase with current, as found by Guangqing et al.[98]. From 2-6 mA, the plasma appears to be unstable, with large variations in T_g between the different samples. After 6 mA the devices appear to behave as expected. More testing at higher currents would be required. However, limitations on the lifetime of the diamond samples at high currents prevent this.

Another source of error is in the fitting. The residual of the fit between the simulation and the experimental results can be seen in figure 3.13. At each absorption peak there is a large residual, indicating the quality of the fit could be improved upon.

T_g for all samples tested was between 400-600 K. This is also in accordance with the findings of others[98,99]. This also proves the plasma was a glow discharge and not an arc 500 K is far too low for the plasma to be an arc discharge.

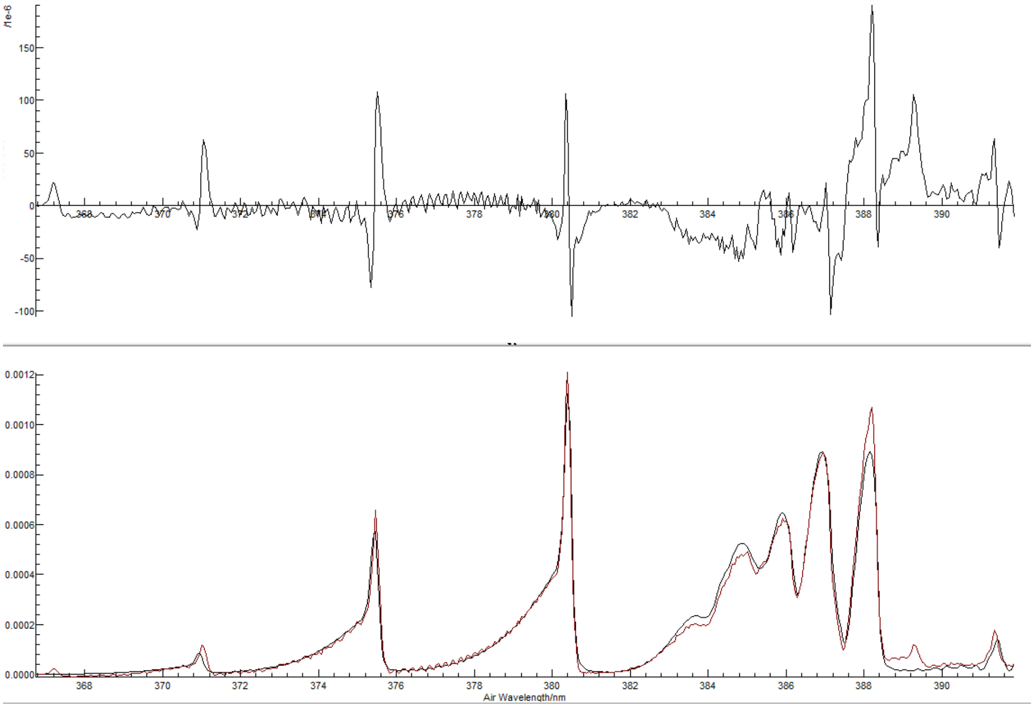

FIGURE 3.13: Residuals for the PGOPHER simulation used to measure rotational temperature.

Chapter 4

Conclusions and Future Work

4.1 Conclusion

Many MHCDs were produced using both diamond and silicon electrodes, with diamond and glass dielectric layers. All configurations were shown to operate stably at pressure ranges of 0.1-9.5 bar, with currents ranging from 0-40 mA.

Whilst the silicon devices were able to operate initially at high currents, and in argon as well as helium, the silicon devices life span was shorter than the diamond samples. The failure modes of the diamond and silicon devices were also explored. In the case of the diamond samples, it was found that the dielectric layer would become coated in a graphite layer, connecting the two electrodes, causing a short circuit. The diamond devices were easily refreshed by washing in concentrated nitric acid. After over 10 hours of use, the silicon samples would not strike easily due to the polycrystalline silicon layer that formed on the surface of the cathode. This layer was porous and formed due to the silicon locally melting and subsequently ejecting from the surface.

The devices were shown via I-V curves to operate in the abnormal, self-pulsing and normal glow modes. These modes were similar to those found for MHCDs at lower pressures, < 1 bar. Paschen curves for all devices were of a higher V_b than predicted from Paschen's law. The curves were also shifted along the $p{\cdot}d$ axis because of the longer electron/ion mean free paths due to hollow cathode.

Gas temperatures for silicon and diamond devices were shown to be 400-600 K using optical emission spectroscopy, consistent with literature values. There was a slight trend of increasing T_g with increasing current.

An array of two slits in diamond was successfully produced. I-V curves showed that the sustaining voltages for the two slits were different, due to the slightly different geometries.

Measurements of a capacitor using a 10 ms chirp were successful. Sheath capacitance for an MHCD device at 3-5 bar calculated to be around 100 nF. However, the errors are too large for this value to be considered reliable. The error is thought to occur because the plasma is not stable over a long enough time period and also because the model assumption, that the microplasma circuit is a capacitor and resistor in parallel, is over simplified.

4.2 Future Work

4.2.1 Sample Fabrication

As no significant difference was found using different materials for the dielectric layer, a large portion of the sample fabrication time could be removed if an intrinsic layer does not need to be grown on the p-type diamond.

The laser cutter limits the minimum size of the hole to around 100 μm. At diameters below 100 μm, the hole becomes blocked during the cutting process, preventing a clean circle from being cut. An alternative milling method, such as laser cutting in pure oxygen atmosphere to convert the diamond to CO_2, would allow smaller values for d to be investigated.

4.2.2 Sample Holder

An alternate sample holder was designed and partially produced. The new sample holder had an aperture through the anode as well, allowing complete gas flow through the device. It would be worth investigating into whether the graphite layer would form with this gas flow and with somewhere for the graphite to accumulate other than at the dielectric-anode interface. This would potentially allow the diamond samples to operate for much longer periods of time. Investigations into the viability with other gases, such as nitrogen and heavier noble gases, would open up the use of diamond for microplasma chemical reactors.

4.2.3 Sheath Length

Updates to the sheath model of a microplasma could allow accurate measurements of the sheath capacitance. This would give a value for the sheath thickness which has not been previously explored or understood for microplasmas at high pressures. An alternative method could be to use spatially resolved optical spectroscopy to detect ion concentrations. This would show the sheath edge and subsequently the sheath thickness, providing the sheath thickness is large enough to be resolved.

4.3 Acknowledgements

Without the help of Dr. Ben Truscott, none of this would have been possible. His constant, intelligent insights helped keep the project moving forward.

My thanks go out to Professor Paul May and Dr. Neil Fox for use of the diamond lab and for establishing this project. Thank you Dr. Mohammad Zamir Othman for your help in growing the diamond samples and Jan Harwood for helping to operate the laser cutter.

Bibliography

[1] *Nonthermal Plasma Chemistry and Physics* ,J. Meichsner et al., CRC Press, London (2013)

[2] *Introduction to Plasma Physics and Controlled Fusion: Volume 1*, F. F. Chen, Springer, Second Edition, Berlin (2006)

[3] *Plasma Physics: Confinement, Transport and Collective Effects*, A. Dinklage et al., Springer, Berlin (2005)

[4] *Principles of Plasma Discharges and Material Processing,* M. A. Lieberman & A. J. Lichtenberg, John Wiley & Sons, New York (1994)

[5] *Fundamentals of Plasma Physics*, P. M. Bellan, Cambridge University Press, New York (2008)

[6] *Advances in numerical modeling of astrophysical and space plasmas*, A. L. Peratt, AP&SS **242** 93 (1996)

[7] *Glow discharge Processes*, B. Chapman, John Wiley and Sons, Toronto (1980)

[8] *Plasma spectroscopy*, J. Cooper, Rep. Prog. Phys. **29** 35 (1966)

[9] *Thermal plasma modelling*, Gleizes et al., J. Phys. D. **38** R153 (2005)

[10] *Removal of Volatile Organic Compounds from Air Streams and Industrial Flue Gases by Non-Thermal Plasma Technology*, K. Urashima & J. S. Chang, IEEE Trans. Dielectr. Electr. Insul. **7** 5 (2000)

[11] *Effective Ozone Generation with a Wire-Wire Type Nonthermal Plasma Reactor with a Slit Barrier*, J. S. Jung & J. D. Moon, IEEE Trans. Ind. Appl. **44** 5 (2008)

[12] *Cross-Sections, Rate Constants and Transport Coefficients in Silane Plasma Chemistry* Perrin et al., Contrib. Plasm. Phys. **36** 3 (2006)

[13] *Plasma processing of municipal solid waste*, E. Leal-Quirós, Braz. J. Phys. **34** 4b (2004)

[14] *The Bohm criterion and sheath formation*, K. U. Reimann, J. Phys. D: Appl. Phys. **24** 493 (1991)

[15] *Plasma Processes for Semiconductor Fabrication*, W. N. G. Hitchon, Cambridge University Press (1999)

[16] *Electrostatic shielding in plasmas and the physical meaning of the Debye length*, G. Livadiotis & D. J. McComas, J. Plasma Physics **80** 341 (2014)

[17] *On the Landau approximation in plasma physics*, R. Alexandrea & C. Villani, Ann. I. H. Poincare C **21** 61, (2004)

[18] *Positive Ion Currents from the Positive Column of Mercury Arcs*, I. Langmuir, Science **58** 1502 (1923)

[19] *Control of an Arc Discharge by Means of a Grid*, A. W. Hull & I. Langmuir, Proc. Natl. Acad. Sci. **15** 3 (1929)

[20] *The characteristics of electrical discharges in magnetic fields: edited by A. Guthrie and R. K. Wakerling*, D. Bohm, The McGraw-Hill Book Co., (1949)

[21] *The Low Pressure Plane Symmetric Discharge*, R. Harrison & W. B. Thompson, Proc. Phys. Soc. **74** 145 (1959)

[22] *Kinetic theory of the presheath and the Bohm criterion*, S. D. Baalrud & C. C. Hegna , Plasma Sources Sci. Technol. **20** 025013 (2011)

[23] *High Frequency Representation of a Plasma Sheath*, J. C. Sprott, University of Wisconsin, Thermonuclear Plasma Studies (1966)

[24] *The excitation structure in a micro-hollow cathode discharge in the normal regime at medium argon pressure*, C. Lazzaroni et al., J. Phys. D: Appl. Phys. **43** 124008 (2010)

[25] *Sheath and electron density dynamics in the normal and self-pulsing regime of a micro hollow cathode discharge in argon gas*, C. Lazzaroni et al., EPJ D **60** 555 (2010)

[26] *Criterion for Townsend breakdown in a crossed electric and magnetic field with wall losses*, A. E. D. Heylen, Int. J. Electronics **41** 209 (1976)

[27] *On the potential difference required for spark initiation in air, hydrogen, and carbon dioxide at different pressures*, F. Paschen, Ann. Phys. **37** 69 (1889)

[28] *Sparking formulae for very high-voltage Paschen characteristics of gases*, A. E. D. Heylen, IEEE Elect. Insul. Mag. **22** 25 (2006)

[29] *High Voltage Engineering (2nd ed.)*, C. L. Waghwa, New Age International, (2007)

[30] *Plasma generation and plasma sources*, H. Conrads & M. Schmidt , Plasma Sources Sci. Technol. **9** 441 (2000)

[31] *Negative Glow Plasma as a Cathode for Electron Tubes*, J. M. Anderson and L. A. Harris, J. Appl. Phys. **31** 1463 (1960)

[32] *Plasma Physics and Engineering*, A. Fridman & L. A. Kennedy, Taylor & Francis, (2004)

[33] *The negative glow and Faraday dark space in near-normal neon discharges*, G. A. Woolsey & et al., Int. J. Electron. **26** 505 (1969)

[34] *Positive Column Plasma in a Neon Discharge at Medium Pressures*, E. I. Toader, Int. J. Electronics **23** 417 (1967)

[35] *Anode glows in glow discharges : outstanding problems*, K. G. Emeleus, Int. J. Electronics **52** 407 (1982)

[36] *The glow discharge at low pressure*, G. Francis, Springer, (1956)

[37] *Plasma Chemistry*, A. Fridman, Cambridge University Press, (2008)

[38] *Low-pressure gas discharge modelling*, G. G. Lister, J. Phys. D: Appl. Phys. **25** 1649 (1992)

[39] *Electrical discharges in gases*, F. M. Penning, Macmillian, (1957)

[40] *Microplasmas and applications*, K. H. Becker et al., J. Phys. D: Appl. Phys. **39** R55 (2006)

[41] *Microplasmas: Sources, Particle Kinetics, and Biomedical Applications*, F. Iza et al., Plasma Process. Polym. **5** 322 (2008)

[42] *Current Status of Microplasma Research*, K. Tachibana, IEEJ T. Electr. Electr. **1** 145 (2006)

[43] *Fundamentals of Gaesous Ionization and Plasma Electronics*, E. Nasser, Wiley (1971)

[44] *Arc erosion behaviour of silver electric contacts in a single arc discharge across a static gap* , R. T. Lee et al., IEE Proc.: Sci., Meas. Technol. **148** 8 (2001)

[45] *Electrical breakdown and ESD phenomena for devices with nanometer-to-micron gaps*, A. Wallash & L. Levit, SPIE **4980** 87 (2003)

[46] *A mathematical model of the modified Paschen's curve for breakdown in microscale gaps*, D.B. Go & D. A. Pohlman, J. Appl. Phys. **107** 103303 (2010)

[47] *Electron Emission at High Fields Due to Positive Ions*, P. Kisliuk, J. Appl. Phys. **30** 51 (1959)

[48] *Cold-cathode discharges and breakdown in argon: surface and gas phase production of secondary electrons*, A. V. Phelps & Z. Lj. Petrovic, Plasma Sources Sci. Technol. **8** R21 (1999)

[49] *Microhollow cathode discharges*, K. H. Schoenbach et al., Appl. Phys. Lett. **68** 13 (1996)

[50] *Analysis of the self-pulsing operating mode of a microdischarge*, Y. X. Aubert et al., Plasma Sources Sci. Technol. **16** 23 (2007)

[51] *Predicted properties of microhollow cathode discharges in xenon*, Y. X. Aubert et al., Appl. Phys. Lett. **86** 071501 (2005)

[52] *Experimental demonstration of the pendulum effect in a cylindrical low-pressure hollow cathode discharge in argon*, H. Helm, Z. Naturf. A **27** 1812 (1972)

[53] *Proof and analysis of the pendulum motion of beam electrons in a hollow cathode discharge*, G. Stockhausen & M. Kock, J. Phys. D: Appl. Phys. **34** 1683 (2001)

[54] *New Hollow Cathode Glow Discharge*, A. D. White, J. Appl. Phys. **30** 711 (1959)

[55] *Studies of the Properties of the Hollow Cathode Glow Discharge in Helium and Neon*, D. J. Sturges & H. J. Oskam, J. Appl. Phys. **35** 2887 (1964)

[56] *Modelling of microdischarge devices: plasma and gas dynamics*, M. J. Kushner, J. Phys. D: Appl. Phys. **38** 1633 (2005)

[57] *Linear, segmented microdischarge array with an active length of 1 cm: cw and pulsed operation in the rare gases and evidence of gain on the 460.30 nm transition of* Xe^+, P. von Allmen et al., Appl. Phys. Lett. **82** 4447 (2003)

[58] M. F. Ashby & D. R. H. Jones, *Engineering Materials: An Introduction to their Properties and Applications*, Pergamon Press, Oxford, (1980)

[59] *Microhollow cathode discharges*, K. H. Schoenbach et al., Appl. Phys. Lett. **68** 1 (1996)

[60] *Ion etching for pattern delineation*, C. M. Melliar-Smith, J. Vac. Sci. Technol. **13** 1008 (1976)

[61] *Microdischarge devices fabricated in silicon*, J. W. Frame et al., Appl. Phys. Lett. **71** 1165 (1997)

[62] *Development and Characterization of Micromachined Hollow Cathode Plasma Display Devices*, J. Chen et al., J. Microelectromech. Syst. **11** 536 (2002)

[63] *Development and Characterization of Micromachined Hollow Cathode Plasma Display Devices*, S. J. Park et al., Appl. Phys. Lett. **86** 111501 (2005)

[64] *Diamond Thin Films: a 21st-Century Material*, P. W. May, Phil. Trans. R. Soc. Lond. A **358** 473 (2000)

[65] *Cold Cathode of p-Type Semiconducting Diamond Films for Gas Discharge*, A. Hatta et al., Plasma Process. Polym. **4** S942 (2007)

[66] *Enhancing the plasma illumination behaviour of microplasma devices using microcrystalline/ultrananocrystalline hybrid diamond materials as cathodes*, T. Chang et al., Nanoscale **5** 7467 (2013)

[67] *Generation of microdischarges in diamond substrates*, S. Mitea et al., Plasma Sources Sci. Technol. **21** 022001 (2012)

[68] *Add Ceramic "MEMS" to the Pallet of MicroSystems Technologies*, D. L. Wilcox et al., Mater. Res. Soc. Symp. Proc. **687** 225 (2002)

[69] *Ceramic microdischarge arrays with individually ballasted pixels*, P. von Allmen et al., Appl. Phys. Lett. **82** 2562 (2002)

[70] *Add Ceramic "MEMS" to the Pallet of MicroSystems Technologies*, D. B. A. Vojak et al., Appl. Phys. Lett. **78** 1640 (2001)

[71] *Microplasma Technology and Its Applications in Analytical Chemistry*, X. Yuan et al., Appl. Spectrosc. Rev. **46** 581 (2011)

[72] *Generation of micrometer-scale discharge in a supercritical fluid environment*, T. Ito & K. Terashima, Appl. Phys. Lett. **80** 2854 (2002)

[73] *Destruction of hydrocarbons in non-thermal, ambient-pressure, capillary discharge plasmas*, A. Koutsospyros et al., Int. J. Mass Spectrom. **233** 305 (2004)

[74] *Plasmochemical Degradation of Volatile Organic Compounds (VOC) in a Capillary Discharge Plasma Reactor*, A. Koutsospyros et al., IEEE Trans. Plasma Sci. **33** 42 (2005)

[75] *Flexible Displays: Sheetlike microplasma arrays have many applications*, G. Eden & S. J. Park, Laser Focus World **46** 33 (2010)

[76] *Microplasma light tiles: thin sheet lamps for general illumination*, G. Eden et al., J. Phys. D: Appl. Phys. **44** 224011 (2011)

[77] *Lighting from thin (<1mm) sheets of microcavity plasma arrays fabricated in Al/Al_2O_3/glass structures*, S. J. Park et al., Phys. D: Appl. Phys. **40** 3907 (2007)

[78] *Smoothing and Differentiation of Data by Simplified Least Squares Procedures*, A. Savitzky & M. J. E. Golay, Anal. Chem. **36** 1627 (1964)

[79] *Wavelengths of spectral lines in mercury pencil lamps*, C. J. Sansonetti et al., Appl. Optics **35** 74 (1996)

[80] *PGOPHER, a Program for Simulating Rotational Structure*, C. M. Western, University of Bristol, http://pgopher.chm.bris.ac.uk

[81] *Spatiotemporal Profile of Emission From Oscillating DC Microdischarges*, T. Kuschel et al., IEEE trans. Plasma Sci. **39** 2692 (2011)

[82] *Oscillation modes of direct current microdischarges with parallel-plate geometry*, I. Stefanović et al., J. Appl. Phys. **110** 083310 (2011)

[83] *Hollow cathode discharges: Volt-ampere characteristics and space-time resolved structure ofthe discharge*, D Marić et al., J. Phys.: Conf. Ser. **162** 012007 (2009)

[84] *Self-pulsing microplasma at medium pressure range in argon*, A. Rousseau1 & X. Aubert, J. Phys. D: Appl. Phys. **39** 1619 (2006)

[85] *Modelling of low-current self-generated oscillations in a hollow cathode discharge*, Z. Donko, J. Phys. D: Appl. Phys. **32** 1657 (1999)

[86] *Calculation of the Townsend Discharge Coefficients and the Paschen Curve Coefficients*, K. T. A. L. Burm, Contrib. Plasma Phys. **47** 177 (2007)

[87] *Microhollow cathode discharge and breakdown in micron separations*, B.N. Sismanoglu & J. Amorim, Eur. Phys. J. Appl. Phys. **41** 165 (2008)

[88] *Temporal limits of a rapidly swept Langmuir probe*, R. B. Lobbia & A. D. Gallimore, Phys. Plasmas **17** 073502 (2010)

[89] *Measurements of the plasma sheath capacitance using a simple tunnel diode oscillator*, B. M. Oliver & R. M. Clements , J. Phys. E: Sci. Instrum. **5** 718 (1972)

[90] *A measurement of the effective thickness of the plasma sheath at a cold electrode*, J. A. Nation & D. Simpson , Br. J. Appl. Phys. **16** 1705 (1965)

[91] *Resonance behavior of the ion sheath capacitance near the plasma ion frequency*, B. M. Oliver & R. M. Clements, J. Appl. Phys. **44** 1128 (1973)

[92] *Experimental investigation of the low frequency capacitive response of a plasma sheath*, B. M. Oliver et al., J. Appl. Phys. **44** 4511 (1973)

[93] *Images of Glow Discharges in Slit Microhollow Cathode*, Y. D. Wang & J. T. Ouyang, IEEE Trans. Plasma Sci. **27** 16 (1999)

[94] *Development and Characterization of Micromachined Hollow Cathode Plasma Display Devices*, J. Chen et al., J. Microelectromech. Syst. **11** 536 (2002)

[95] *Modelling of microdischarge devices: plasma and gas dynamics*, M. J. Kushner, J. Phys. D: Appl. Phys. **38** 1633 (2005)

[96] *Gas Chemistry Related to the Operation of Microhollow Cathode Discharges*, V. Felix et al., GD2014 (2014)

[97] *In-situ observation of surface blistering in silicon by deuteriumand heliumion irradiation*, S. Igarashi et al., Surf. Coat. Tech. **158** 421 (2002)

[98] *Experimental Investigation of Microhollow Cathode Discharge for the Application to Microplasma Thrusters*, X.I.A. Guangqing et al., Tsinghua Sci. Technol. **14** 49 (2009)

[99] *Measurement of rotational temperatures in high-pressure microhollow cathode (MHC) and capillary plasma electrode (CPE) discharges*, S. Igarashi et al., Acta Physica Slovaca **54** 115 (2004)

[100] *Pressure Dependences of Gas Temperature and Electron Density in Microhollow Cathode Discharges in He and He+*H_2O *Gases*, T. Yamasak et al., Jpn. J. Appl. Phys. **51** 126101 (2012)

[101] *Emission spectroscopy of a microhollow cathode discharge plasma in helium-water gas mixtures*, S. Namba et al., J. Appl. Phys. **110** 073307 (2011)

[102] *Gas temperature determination from rotational lines in non-equilibrium plasmas: a review*, P. J. Bruggeman et al., Plasma Sources Sci. Technol. **23** 023001 (2014)